The non-hydrostatic global atmospheric model for CMIP6 HighResMIP simulations (NICAM16-S): Experimental design, model description, and sensitivity experiments

Chihiro Kodama[1], Tomoki Ohno[1], Tatsuya Seiki[1], Hisashi Yashiro[2], Akira T. Noda[1], Masuo Nakano[1], Yohei Yamada[1], Woosub Roh[3], Masaki Satoh[3,1], Tomoko Nitta[3], Daisuke Goto[2], Hiroaki Miura[4], Tomoe Nasuno[1], Tomoki Miyakawa[3], Ying-Wen Chen[3], and Masato Sugi[5]

[1]Japan Agency for Marine-Earth Science and Technology, Yokohama, 236-0001, Japan
[2]National Institute for Environmental Studies, Tsukuba, Ibaraki, 305-8506, Japan
[3]Atmosphere and Ocean Research Institute, The University of Tokyo, Kashiwa, 277-8564, Japan
[4]Department of Earth and Planetary Science, Graduate School of Science, The University of Tokyo, Tokyo, 113-0033, Japan
[5]Meteorological Research Institute, Tsukuba, 305-0052, Japan

Correspondence to: Chihiro Kodama (kodamac@jamstec.go.jp)

Submitted to *Geoscientific Model Development* (29 December 2019)

Abstract. NICAM, a nonhydrostatic global atmospheric model with an icosahedral grid system, has been developed for nearly two decades. This paper describes NICAM16-S, the latest stable version of NICAM (NICAM.16) modified for Coupled Model Intercomparison Project Phase 6 (CMIP6). Major updates from NICAM.12, a previous version used for climate simulations, include updates of a cloud microphysics scheme and a land model, an introduction of natural and anthropogenic aerosols and a subgrid-scale orographic gravity wave drag, and improvement of coupling between cloud microphysics and radiation schemes. External forcings were updated to follow a protocol of CMIP6 High Resolution Model Intercomparison Project (HighResMIP). A series of short-term sensitivity experiments were performed to check and understand impacts of the model updates on the simulated mean states. Improvements in the ice water content, the high cloud amounts, the surface air temperature over the Arctic region, the location and the strength of zonal mean subtropical jet, and shortwave radiation over the Africa and the South Asia were found in the NICAM16-S simulations. Some long-standing biases such as the double intertropical convergence zone and smaller low cloud amounts still exist or even worsen in some cases, suggesting further necessity for understanding their mechanisms and upgrading schemes and/or their parameter settings as well as for enhancing horizontal and vertical resolutions.

1. Introduction

Moist processes play a crucial role in the formation of the Earth's climate. The moist convection redistributes the mass, energy, and momentum of the atmosphere to form large-scale circulation. Clouds are coupled with large-scale circulation

through latent and radiative heating, which can affect climate sensitivity. Natural disasters, including heavy precipitation and strong wind associated with tropical and extratropical cyclones, are heavily involved in the moist processes.

Considering the importance of fine-scale moist processes, increasing the spatial resolution of the global atmospheric model

5   may be a straightforward approach to improving climate simulations (Kinter et al., 2013; Roberts et al., 2018; Satoh et al., 2019; Shukla et al., 2009). This motivated us to perform the first cloud-system resolving climate simulations of the present-day and the future using a 14 km mesh non-hydrostatic global atmospheric model (NICAM; Satoh et al., 2008, 2014; Tomita and Satoh, 2004). Kodama et al. (2015) and Satoh et al. (2015) provided brief descriptions of the model (hereafter referred to as NICAM.12) and experimental design of the climate simulations. This unique high-resolution climate dataset, whose

10 overall performance was reported in Kodama et al. (2015), has been used in many studies, focusing on tropical cyclones (Matsuoka et al., 2018; Satoh et al., 2015, 2018; Sugi et al. in prep.; Yamada et al., 2017, 2019), extratropical cyclones (Kodama et al., 2019; McCoy et al., 2019; Satoh et al., 2018), intraseasonal oscillations including Madden–Julian Oscillation (MJO) (Kikuchi et al., 2017; Nakano and Kikuchi, 2019), tropical synoptic-scale waves (Fukutomi et al., 2016), cloud radiative feedback (Chen et al., 2016; Noda et al., 2019; Satoh et al., 2018), and regional-to-global precipitation (Kilpatrick

15 et al., 2017; Na et al., submitted.; Satoh et al., 2018; Takahashi et al., submitted).

Also, some significant climate biases have been identified in the simulation (Kodama et al., 2015), and great efforts have been devoted to improving the model for better performance of the simulated climate in a physically-consistent manner. Major updates between NICAM.12 and NICAM.16, a stable version of NICAM released in 2017, are an update of the cloud

20 microphysics scheme based on a comparison with Tropical Rainfall Measuring Mission (TRMM) satellite observation (Roh et al., 2017; Roh and Satoh, 2014), an introduction of a wetland scheme in a land model (Nitta et al., 2017), an implementation of the coupling between cloud microphysics and radiation that considers the nonsphericity of ice, and a subgrid-scale orographic gravity wave drag scheme. In addition, some parameters related to the processes of surface albedo and sea ice have been revised. NICAM.16 has been further modified to conform to the Coupled Model Intercomparison

25 Project Phase 6 (CMIP6) High Resolution Model Intercomparison Project (HighResMIP) protocol (Haarsma et al., 2016). That is, the interfaces of the CMIP6 external forcings (natural and anthropogenic aerosols and the solar cycle) have been implemented. This special version of NICAM.16 for CMIP6 is labeled NICAM16-S, where "-S" represents the use of a single-moment cloud microphysics scheme. These model updates often (but not always) reduce the biases of the simulated mean states, as reported later.

This section has provided a summary of the description of NICAM16-S with a focus on the differences from NICAM.12. Section 2 of this paper presents the experimental design (resolutions as well as initial and boundary conditions) of the HighResMIP simulations and a series of sensitivity experiments by NICAM16-S. Section 3 explains the detailed model updates of NICAM16-S from NICAM.12 and their impacts on the simulated mean states. Section 4 presents the preliminary

evaluations of the mean states simulated by NICAM16-S. Section 5 reports on the computational aspects of the simulation. Section 6 provides a quick summary of this paper.

2. Experimental design

2.1 Spatial and temporal resolutions

Three sets of model configurations were prepared for the HighResMIP simulations and initial and boundary conditions were made for each. NICAM16-S with specific horizontal resolutions were formally labeled NICAM16-7S (56 km mesh), NICAM16-8S (28 km mesh), and NICAM16-9S (14 km mesh). The horizontal mesh size is evaluated as a square root of the mean area of each grid cell (Satoh et al., 2014). The number n in NICAM17-nS is a grid division level (glevel), which denotes a number of subdivisions of the icosahedron to generate a mesh (Tomita et al., 2001). The physics schemes, including parameters, and the initial and boundary conditions are common among different horizontal resolutions except for those explicitly noted in Sections 2 and 3.

The number of vertical levels is 38, with a model top height of around 40 km, equivalent to the previous climate simulations (Kodama et al., 2015). Atmospheric phenomena of interests may be practically well simulated including the tropical cyclones, MJO, and diurnal precipitation cycle, as we have confirmed in the previous study (Kodama et al., 2015), though the vertical resolution is not sufficient to resolve the cirrus clouds (Seiki et al., 2015b) and atmospheric gravity waves (Watanabe et al., 2015).

The time step intervals for the dynamical process are set to 240, 120 and 60 s for NICAM16-7S, NICAM16-8S, and NICAM16-9S, respectively. Diffusion coefficients of the divergence damping, the second-order Laplacian background horizontal diffusion, and the first-order Laplacian horizontal diffusion for sponge layer above 20 km are reduced appropriately as the horizontal resolution is increased (Satoh et al., 2008). The time step interval of the cloud microphysics scheme is 30 s and that of the surface processes including turbulence is 60 s for all the horizontal resolutions. The radiation scheme, which requires considerable computational time, is executed every 40, 20, and 10 min for NICAM16-7S, NICAM16-8S, and NICAM16-9S, respectively.

2.2 Initial conditions

Table 1 shows the integration periods of the HighResMIP simulations. For the Tier 1 simulations, which start from 1 January 1950, the initial condition of the atmosphere was taken from the ERA-20C reanalysis (Poli et al., 2016). Strictly following the HighResMIP protocol, the simulations continued until 31 December 2014, using NICAM16-7S and NICAM-8S. The

HighResMIP Tier 3 simulations using NICAM16-7S and -8S started from 1 January 2015 as a continuation of the Tier 1 simulations and ended on 31 December 2050. Higher computational cost hinders us from running NICAM16-9S for a hundred years, and thus a time-slice approach is adopted, instead. Specifically, climate simulations have been performed in the following timeframes: 1950–1960, 2000–2010, and 2040–2050. The initial land condition in the past and present-day

5   simulations was taken from a monthly mean climatology of the simulation by NICAM with a mesh size of 220 km (glevel-5) under a present-day condition. It was performed for 10 years, and the last 5 year data were used to obtain the monthly mean land climatology. This approach is the same as the one used in the previous climate simulations (Kodama et al., 2015). The initial land condition for the future time slice run with a 14 km mesh was obtained by interpolating the output of the 28 km mesh run.

In addition to the formal HighResMIP simulations, we performed a series of short-term sensitivity experiments to evaluate impacts of the model updates on the simulated climatology, as listed in Table 2. Here, the model configuration of the experimental ID "g" is equivalent to that used in the HighResMIP Tier 1 and 3 simulations, and all the other configurations of the sensitivity experiments are the derivative of "g", as described in Table 2. These experiments were performed from the

15   initial condition beginning from 1 June 2004 because it was used frequently in the previous NICAM studies (e.g., Kodama et al., 2012; Noda et al., 2016; Seiki et al., 2015a). The integration periods of these sensitivity experiments are 1 year in most cases.

2.3 External forcings

20   External forcings of the simulations basically followed the HighResMIP protocol (Haarsma et al., 2016); in other words, historical and SSP585-scenario forcings (O'Neill et al., 2016) were used in the Tiers 1 and 3 simulations.

Daily quarter-degree sea surface temperature (SST) and sea ice mass (ICE) prescribed for the model were obtained from HadISST 2.2.0.0 (Kennedy et al., 2017; Kennedy et al., The Met Office Hadley Centre Sea Ice and Sea-Surface Temperature

25   data set, version 2.2.0.0, Technical Note, in prep). SST dataset is extended from 2016 to 2050 using a trend obtained from a CMIP5 model ensemble mean following the RCP8.5 scenario and historic variability from 1980 to 2015 (Kennedy et al., 2019). Since HadISST provides historical sea ice concentration (SIC), ICE was diagnosed from SIC for NICAM (see Section 3.6). Future SIC is estimated from the future SST data and an observed relationship between SST and SIC (Kennedy et al., 2019; https://github.com/PRIMAVERA-H2020/HighResMIP-futureSSTSeaice). Both the SST and ICE were fixed to the

30   boundary conditions in the HighResMIP Tiers 1 and 3 simulations. In the short-term sensitivity experiments, a slab ocean model with a nudging toward the prescribed SST was also tested for a practical purpose (see Section 3.6 for its impact on the simulated climate). In the sensitivity experiments, the fixed SST condition was used in 56 km mesh run whereas and the slab ocean model with the nudging was used in 14 km mesh runs unless explicitly specified.

Figure 1 and Figure 2 display the decadal mean SST and ICE prescribed for the model; Figure 3 exhibits their global-mean variability. Greater warming over the maritime continent, the Indian Ocean, and the edge of the polar regions are found in the 2000s compared with the 1950s, whereas cooling is noticed in the North Pacific and the North Atlantic. Future change in

5   SST is somewhat similar to the El Niño pattern, and the warming is also prominent in the midlatitudes, the tropical Atlantic Ocean, and the edge of the polar regions. Similar tendencies are observed for the distribution of SST trend (not shown). The global mean SST is 17.9 °C in the 1950s, 18.2 °C in the 2000s, and 19.0 °C in the 2040s. ICE continues to decrease from the past to the future. The global mean ICE is anearly halved by the 2040s compared with that in the 1950s.

10   The global annual mean of greenhouse gas (GHG) concentrations (Meinshausen et al., 2017; Meinshausen and Nicholls, 2018; Meinshausen and Vogel, 2016) was prescribed for the model. Specifically, CO_2, CH_4, N_2O, CFCs (CFC-12, CFC-11, CFC-113, CFC-114, and CFC-115), HCFCs (HCFC-22, HCFC-141b, and HCFC-142b), HFCs (HFC-134a, HFC-32, HFC-125, HFC-143a, and HFC-152a), CCl_4, CF_4, SF_6, and C_2F_6 are considered as GHG concentrations. Also, historical and future monthly concentrations of the three-dimensional ozone field (Hegglin et al., 2016, 2018, in prep.) were prescribed.

Natural aerosol mass and the number concentration prescribed for the model were obtained from a low-resolution NICAM simulation with online aerosol module based on the Spectral Radiation-Transport Model for Aerosol Species (SPRINTARS) (Takemura et al., 2000, 2002, 2005, 2009; Goto et al., 2008, 2011). The simulated climatology of the aerosol in NICAM has been validated (Goto et al., 2018; Suzuki et al., 2008). For CMIP6, NICAM with 220 km mesh (glevel-5) was performed for

20   100 years using natural aerosol emission with the anthropogenic aerosol module MACv2-SP (Fiedler et al., 2018; Stevens et al., 2017; see Section 3.3) under a perpetual 2012 condition, and the data of the last 90 years were averaged to obtain a monthly-mean climatology of aerosol mass concentration and number concentration of cloud condensation nuclei (CCN) from a natural origin. A low-bound limiter of 50 cm^{-3} was applied to the CCN prescribed for the model to avoid numerical instability in the cloud microphysics scheme. Figure 4 shows the annual means of the natural aerosol optical thickness and

25   CCN simulated by and prescribed to the model[1]. The climatology of natural aerosol mass and CCN is invariant year by year, whereas anthropogenic aerosol from MACv2-SP is time-dependent in the historical and future simulations (Fiedler et al., 2019; Stevens et al., 2017). Further, aerosol optical properties were overwritten with the stratosphere aerosol dataset (Thomason et al., to be submitted) above the tropopause to introduce effect of volcanic eruptions on the radiation field in a consistent way among different models participating in CMIP6.

---

[1] Note that an error was found in the natural aerosol forcing prescribed to the model, as recently reported in ES-DOC Errata website (https://errata.es-doc.org/static/view.html?uid=ada34e91-4a94-d668-a491-fe16556aaf46). Its influence on the results presented in this paper seems to be negligible, according to an additional 56 km mesh experiment with the corrected natural aerosol forcing (not shown).

Similar to the implementation of MIROC6 (Tatebe et al., 2019), historical monthly mean solar forcings (Matthes et al., 2017b, 2017a) were prescribed as total solar irradiance and solar irradiance spectra in the radiative scheme MstrnX (Sekiguchi and Nakajima, 2008). In terms of land processes, the monthly climatology (2004–2013) of leaf area index (LAI)
5   was obtained from Moderate Resolution Imaging Spectroradiometer (MODIS) product (MCD15A2.005: Shabanov et al., 2005; Yang et al., 2006).

As briefly noted in Satoh et al. (2014), a smoother is applied to the model topography to avoid a model abort due to numerical instability. Specifically, a hyper-diffusion is repeatedly applied to the GTOPO30 (doi:10.5066/F7DF6PQS), a
10   global digital elevation model with a horizontal spacing of approximately 1 km, to meet a certain criterion of maximum elevation gradient. The maximum elevation gradient is set to 0.01, 0.01414, and 0.02 mm^{-1} for NICAM16-7S, NICAM16-8S, and NICAM16-9S, respectively, and is called "A-topography". Note that, in previous NICAM studies using 14 km horizontal mesh (e.g., Kodama et al., 2015), "B-topography", in which A-topography of 28 km mesh was interpolated to 14 km mesh grid point, was often used for the sake of stable integration. For CMIP6, A-topography was used to better
15   represent steeper mountains and their effects on the atmospheric phenomena.

3. Model description and impact of model updates on the simulated fields

Table 3 shows a summary of the physics schemes used in NICAM16-S and NICAM.12. Dynamical core and horizontal and vertical diffusion, including the planetary boundary layer schemes in NICAM16-S, are the same as those of NICAM.12
20   except for some minor updates. A cloud microphysics scheme is used instead of a combination of convection and large-scale condensation schemes to explicitly represent interactions between clouds and circulation. Although most climate models continue to use convection and large-scale condensation schemes even for a mesh size around 14 km, we believe that being free from development and tuning of such complex parameterizations can be another wise option to focus more on investigating the nature of the simulation with explicit cloud microphysics when we expect to proceed toward global cloud
25   resolving climate simulation in the future. Furthermore, global mean precipitation is constrained by radiative cooling in a large-scale clear-sky regions, which can be captured by the relatively coarse resolution run. Although our choice leads to a patchy behaviour of precipitation in the simulation, the simulated climatology of the precipitation pattern, even by the lowest resolution setting (NICAM16-7S), is comparable with the observation (see Section 4).

30   A series of short-term sensitivity experiments were performed to monitor impacts of several model updates on the simulated climatology. Table 2 offers a full list of sensitivity experiments, and Table 4 presents observations for comparisons with the model . Some of their impacts on the global means are summarized in Table 5, and comparisons with observations along

with impacts of the horizontal resolutions are shown in Table 6 for reference. Unless explicitly specified, the simulation data are re-gridded to the same grid of observations Table 4 or to 2.5° in latitude and longitude. As noted in Section 3.6, we often prefer to use a slab ocean model with nudging toward the boundary SST rather than the fixed SST condition requested by the HighResMIP protocol because of better performance in the simulated precipitation pattern (Kodama et al., 2015). Therefore,

5   both the fixed SST and slab ocean configurations were tested in the sensitivity experiments (see Section 3.6).

3.1 Cloud microphysics

Climate simulations with NICAM16-S were performed with a single moment bulk cloud microphysics scheme with six water categories (hereafter referred to as NSW6). Recently, Roh and Satoh (2014) and Roh et al. (2017) have significantly

10   revised the NSW6 scheme based on comparisons with the TRMM observation. We used the revised version of the NSW6 to show the improvements in the climatology of the NICAM simulation.

The NSW6 scheme was originated with Lin et al. (1983) and Rutledge and Hobbs (1984). After their works, Tomita (2008) modified their cloud microphysics scheme to ensure consistency with thermodynamics used in NICAM; Tomita also

15   simplified it to reduce calculation cost for global high-resolution simulations. The NSW6 was evaluated by comparing the simulated optical properties with satellite observations (Satoh et al., 2010; Kodama et al., 2012; Hashino et al., 2013, 2016; Roh and Satoh, 2014, 2018; Roh et al., 2017) using satellite simulators (CFMIP Observational Simulator Package developed by Haynes et al., 2007; Chepfer et al., 2008; Bodas-Salcedo et al., 2008, 2011, or Joint Simulator developed by Matsui et al., 2009; Masunaga et al., 2010; Hashino et al., 2013). It was revised in each stage of the version management of NICAM

20   (Kodama et al., 2012; Roh and Satoh, 2014; Roh et al., 2017). The revision of the NSW6 scheme by Roh and Satoh (2014) and Roh et al. (2017) is the key in this updated version of the NICAM (NICAM16-S).

Table 7 summarizes key changes in the NSW6 scheme by Roh and Satoh (2014) and Roh et al. (2017) . In short, the revision aimed to enhance organizations of tropical convective cloud systems by assuming lighter precipitation of graupel and snow

25   and by moderately developing cloud ice. Finally, they achieved successful reproduction of the vertical structures of shallow, congestus, and deep convective clouds over the tropics, comparing to TRMM and CloudSat satellite observations. They also used microwave satellite observations to evaluate the simulated results (Roh and Satoh, 2018); hence, improvements in tropical cloud systems with the revised scheme are robust in terms of optical signals (see the original papers for more details). Note that a separation of convective and stratiform systems in Roh and Satoh (2014) was omitted in this study because of its

30   small impact (not shown) despite the high computational cost.

Table 5a shows the global mean impact of the updated cloud microphysics scheme on the simulated mean values. The most noticeable impact is on an increase in ice water content by more than twice, and this mostly accounts for a snow category in

the cloud microphysics scheme. Figure 5 shows the meridional-height cross section of the observed and simulated zonal mean ice water content (IWC) and its breakdown into the categories of cloud ice, snow and graupel in the simulation. The simulated IWC is largely underestimated using the model before the update of cloud microphysics scheme, as also shown in Seiki et al. (2015a), and it becomes comparable with the CloudSat observation after the update. A noticeable increase in the

5 snow category is seen in the tropical upper troposphere and storm-track region. Cloud ice and graupel are also increased in the upper troposphere, and graupel is rather decreased in the storm-track region. As a result, global mean column-integrated cloud ice and snow are increased by 24 % and 399 % and that of graupel is decreased by 8.4 %. The increase in IWC is consistent with the decelerated development of ice water content by the modified mass and diameter relationship of snow, that reduces the snow density (Table 7d), by the diminished efficiency of accretion of cloud ice by snow (Table 7g), and by

10 ignoring an accretion of snow and cloud ice by graupel (Table 7f). Differences in cloud processes (convection vs. synoptic system) may vary increasing/decreasing in graupel by the model update.

Despite the drastic increase in mass concentrations of snow and cloud ice, the amount of high cloud, particularly, optically thin cloud, is somewhat reduced. Consistently, global mean OLR is increased by about 4 W m^{-2} (Table 5a), opposite to that

15 found in Roh et al. (2017). In addition, decrease in TOA brightness temperature by the update (Figure 6) is very small compared with that in Roh et al. (2017). These differences between Roh et al. (2017) and this study can be mostly explained by the new coupling procedure between cloud microphysics and radiative transfer as described in Section 3.2 and be partially explained by the different treatment of terminal velocity of cloud ice. The cloud ice terminal velocity diagnosed by Heymsfield and Donner (1990) was replaced with zero in Roh et al. (2017) whereas it was zero and unchanged in this study.

20 The reduction of the cloud ice fall speed, as in Roh et al. (2017), could increase and elevate the high cloud and decreases the OLR, as also seen in Kodama et al. (2012). A low cloud amount is increased as a result of compensation between an increase in a medium and a thick cloud and a decrease in a thin cloud. These results indicate that the clouds grow thicker on average by updating the cloud microphysics scheme in this study.

25 **3.2 Coupling between cloud microphysics and radiative transfer**

In NICAM16-S, cloud microphysics schemes are fully coupled with a broadband radiative transfer model named MstrnX (Sekiguchi and Nakajima, 2008). The effective radii r_e of hydrometeors are calculated with the same assumption of the particle size distribution function as cloud microphysics. including indirect effect, and then passed to the MstrnX. In contrast, fixed effective radii were assumed in NICAM.12 (8 and 40 μm were assumed for liquid and solid hydrometeors,

30 respectively).

The use of consistent assumptions between cloud microphysics and radiative transfer can reduce a model bias in the radiation budget (Seiki et al., 2015a) and has non-negligible impacts on a climate projection (Chen et al., 2016). In addition,

the coupling provides model developers with a better understanding of the origins of model biases (Hashino et al., 2016). The following section summarizes the changes in the radiation budget by the coupling between cloud microphysics and radiative transfer as well as details of the update.

5   The MstrnX requires the database of single scattering properties of hydrometeors (RADPARA), such as the volume extinction coefficient, absorption coefficient, asymmetry factor, and the second moment of phase function (Nakajima et al., 2000). In NICAM.16 we use the RADPARA database revised by Seiki et al., (2014). The RADPARA database of liquid hydrometeors was pre-calculated according to the Mie theory. The non-spherical RADPARA database developed by Fu (1996) and Fu et al. (1998) was applied to solid hydrometeors. The RADPARA database was then compiled as a lookup
10 table of the effective radii from 1 μm to 1 mm to cover size range of most of the hydrometeors in global simulations (Seiki et al., 2014). The effects of precipitating hydrometeors on the radiation budget are detectable specifically over the intertropical convergence zone (ITCZ) and storm-track region (e.g., Chen et al., 2018; Li et al., 2014, 2016; Michibata et al., 2019; Waliser et al., 2011). The revised RADPARA database was evaluated in depth by comparing it with balloon-borne sonde observations in a midlatitude cirrus case (Seiki et al., 2014), and its effectiveness for global simulations was evaluated in
15 several studies (Satoh et al., 2018; Seiki et al., 2015a, 2015b).

Because of non-sphericity, the effective radius of ice particles has a controversial definition, whereas the effective radius is well defined in the case of spherical particles. According to Fu (1996), the effective radius of solid hydrometeors is defined as follows:

$$r_{e,j} = \frac{3}{4\rho_{ice}} \frac{\rho q_j}{\int_0^\infty A_j(D_j) N_j(D_j) dD} \quad (j = i, s, g), \qquad (1)$$

20 where $j = i, s, g$ are cloud ice, snow, and graupel, ρ is the air density, A_j is the projected area of a particle to flow, and $\rho_{ice} = 916.7$ kg m^{-3}. The integral in equation (1) is analytically calculated using the assumed particle size distribution functions and sponge-like spherical shape in the case of cloud ice and graupel. In contrast, snow has two-dimensional fractal shapes; hence, the numerator-denominator ratio becomes almost constant. Thus, the effective radius of snow is assumed to be constant ($r_{e,j} = 125$ μm with $A_s = 0.45 D_s^{2.0~0}$), which is derived by approximating the *A-D* relationship of aggregates
25 compiled by Mitchell (1996).

The impacts of the coupling procedure and non-spherical scattering were examined by comparing a set of seasonal simulations with NICAM-16S (g run in Table 2), NICAM-16S except for the spherical RADPARA database (g9 run in Table 2), and NICAM-16S except for the fixed effective radii and the spherical RADPARA database (g9a in Table 2).
30 Figure 7 shows the zonal mean values of the OLR and the reflected shortwave radiation (OSR) at TOA from the sensitivity experiments. Given the substantial increase in cloud ice and snow from the new NSW6 (cf. Section 3.1), ice optical thickness increases proportionately to the increases in the ice water path (IWP) with the fixed effective radii. As a result, the

radiation budget for both the longwave and shortwave is strongly biased in the g9a run. A major portion of the biases is drastically offset in the g9 run by assuming larger effective radii in the coupling procedure. Thus, the coupling procedure automatically prevents artificial biases originating from the inconsistent parameter settings between the cloud microphysics and radiative transfer at the model update. The use of the non-spherical RADPARA database slightly increases OSR over the

5 tropics to the midlatitude of the summer hemisphere because the assumed asymmetry factor for non-spherical particles is smaller than the one for spherical particles (cf. Seiki et al., 2014).

Finally, NICAM16-S shows strong negative biases in OLR over the tropical to subtropical regions and OSR over the polar region and subtropical high-pressure belt. The former biases can be solved by increasing vertical resolution to 400 m near the

10 tropopause with 74 vertical layers (Seiki et al., 2015b). The latter biases mainly stem from the underestimation of low-level clouds since the current updates in cloud microphysics do not work on improvements in warm clouds. The coupling procedure strengthens the negative biases become stronger in the midlatitudes (30°N–60°N) (see g9 and g9a runs in Figure 7) because, in NICAM-12, high clouds associated with extratropical cyclones are artificially brightened and, therefore, conceal the biases due to low-level clouds (cf. Fig. 4 in Kodama et al., 2012).

3.3 Aerosols in the cloud microphysics and radiation schemes

In NICAM.12, the direct radiative effect of the aerosol is not considered in the radiation scheme, and the number concentration of CCN is set to a constant value of 50 cm^{-3}, a typical value over the ocean, in the cloud microphysics scheme. In NICAM16-S, both aerosol's direct and indirect effects are considered by prescribing a distribution of aerosol mass

20 concentration in the radiation scheme and CCN in the cloud microphysics scheme. The natural and stratospheric aerosol data has been described in Section 2.3. For anthropogenic aerosol, a simple plume model, MACv2-SP (Fiedler et al., 2019; Stevens et al., 2017) is used to diagnose the following: (a) a vertical profile of the aerosol optical depth, the single scattering albedo (SSA), and the asymmetry factor and (b) a factor of CCN increase arising from anthropogenic aerosol. This means that the magnitude of the anthropogenic increase in CCN depends on that from the natural origin. Above the tropopause,

25 where volcanic eruptions are major sources of aerosol, the extinction coefficient, SSA, and the asymmetric factor are directly prescribed as CMIP6's external conditions (Section 2.3).

Figure 8 and Table 5b show an impact of the above updates concerning natural and anthropogenic aerosols on the simulated radiation field. The update reduces the downward shortwave radiation at the surface over most of the continent, particularly

30 over Africa and South Asia, leading to a reduction of an excess of the insolation there (not shown). The reduced insolation at the surface is partly cancelled out by a reduction in the upward longwave radiation over the Africa in association with a decrease in surface air temperature. An enhancement of the surface downward shortwave radiation is dominant over the ocean in association with a thinning of cloud optical depth and a decrease in cloud amount, particularly in the NICAM16-9S

simulation (not shown). As a result of these compensations, the global mean net surface radiation change arising from aerosol forcing is around –2 W m^{-2} in NICAM16-7S and +0.4 W m^{-2} in NICAM16-9S in this study.

3.4 Land model

5   A land model named as minimal advanced treatments of surface interaction and runoff (MATSIRO; Takata et al. 2003) is used in NICAM. Recently, a wetland scheme was implemented in MATSIRO to represent the storage of snowmelt while considering the subgrid-scale terrain complexity (Nitta et al., 2017); it was implemented in NICAM.16-S. The wetland scheme reduces summertime warm and dry bias over much of Western Eurasia and North America through delayed snowmelt runoff in MIROC5 (Nitta et al., 2017). In addition, effect of a decrease in surface albedo associated with the
10   accumulation of water on land ice was implemented in NICAM.16-S.

Figure 9 shows impacts of the land model update on soil moisture, precipitation, and surface air temperature in boreal summer. The soil moisture is increased over most of the Eurasian and the North American continents as expected from Nitta et al. (2017), particularly in the Siberia and the area around the Great Lakes. Consistently, albeit noisier, precipitation is
15   increased and surface air temperature is decreased on average in the Siberia and the area around the Great Lakes in summer. Longer integration is needed to assess these impacts quantitatively.

3.5 Surface albedo

Surface albedo values were revised based on the observations. In the past, they were tuned to reduce TOA radiation
20   imbalance, which caused a higher bias of surface albedo over the Arctic compared with a satellite observation (Hashino et al., 2016). Table 8 shows the revised and previous values of surface albedo used in NICAM. In most cases, the albedo values are set to be smaller in NICAM16-S than those in NICAM.12. In addition to the changes in Table 8, the elevated ocean surface albedo for the direct visible wave by 1.35 times for the radiation calculation in the previous simulations is discarded in NICAM16-S because this is a highly artificial factor.

Consistent with the reduced albedo and the increased net upward shortwave radiation, sensitivity experiments using NICAM16-7S show that the use of the new albedo configuration tends to reduce the surface air temperature bias over the land ice compared with the old one (Figure 10a vs. Figure 10b and black vs. green lines in Figure 10d). Specifically, the cold bias in Greenland, the Himalayas, and the Antarctic is reduced. Upward net longwave radiation at the surface is decreased
30   over the ocean, consistent with the increased surface albedo for infrared (i.e., less blackbody) over the ocean. Warm bias still exists in the Arctic in the new configuration, and this will be reduced by changing a sea ice configuration, as explained in Section 3.6.

3.6 Treatment of ocean

A mixed-layer slab ocean model similar to McFarlane et al. (1992) had been implemented in NICAM. The model predicts SST, ICE, snow over sea ice, and snow temperature by solving a heat balance between ocean, sea ice, snow, and the atmosphere. A depth of the slab ocean model is set to 15 m, considering the better performance of the simulated precipitation pattern (Kodama et al., 2015) and MJO (Grabowski, 2006). A simple nudging technique is used to force the predicted SST toward a reference SST with a relaxation time of 7 days. In the slab ocean model implemented in NICAM.12 and NICAM.16, SIC is diagnosed from ICE, as,

$$SIC = \begin{cases} \sqrt{\dfrac{ICE}{SICCRT}}, & ICE < SICCRT \\ 1, & ICE \geq SICCRT \end{cases} \tag{2}$$

where SICCRT is set to 300 kg m^{-2}.

In many cases including the HighResMIP protocol, only the SST and SIC data are provided from CMIP6 to run the model, and, therefore, the ICE data prescribed for the model should be diagnosed from SIC. In NICAM.12 and NICAM16-S, ICE is diagnosed simply as,

$$ICE = SICCRT \times SIC^2. \tag{3}$$

In the previous study using NICAM.12, we often set a value of SICCRT to 300 kg m^{-2} for Eq. (3), the same as that used in Eq. (2). However, this situation causes an underestimation of ICE over most of the sea ice areas and leads to a warm bias over the Arctic (Kodama et al., 2015). Based on an ocean model result (Tatebe, personal communication) and sensitivity experiments (Figure 10c), SICCRT is set to 1,600 kg m^{-2} for Eq. (3) in NICAM16-S to diagnose ICE from SIC.

In the HighResMIP protocol, SST and SIC in the model are fixed to the time-varying external conditions. This fixed SST/SIC condition is achieved by nudging SST and ICE toward the prescribed external condition with a zero-relaxation time in the slab ocean model. However, fixed SST simulation is known to cause severe bias in the precipitation pattern in the tropics (Kodama et al., 2015), and thus the use of the slab ocean model with a 7 day relaxation time is often preferred. Table 5e and Figure 11 summarize the comparisons of the simulations between the fixed SST condition and the slab ocean model and nudging. Overall, the global mean impact of the slab ocean model is not very large. In the simulation with slab ocean model, global mean precipitation shows a slight increase and OLR shows an increase, which is associated with a slightly warmer surface air temperature. The introduction of the slab ocean model considerably affects the horizontal distribution of the cloud and precipitation system. Double ITCZ bias is more prominent in the precipitation, high cloud fraction, and OLR fields in the fixed SST runs compared with the slab ocean runs, particularly in the high-resolution run. As far as our

investigation shows, NICAM16-9S with the slab ocean model best simulates the ITCZ peak precipitation and precipitation pattern. Although an importance of the short-term SST variation driven by the atmosphere on the pattern of the precipitation is apparent from Figure 11, the introduction of the slab ocean model alone does not resolve the bias of the precipitation pattern. Further analysis is necessary to understand the physical mechanisms of the bias, notably perhaps the timescale of the convection,.

3.7 Orographic gravity wave drag

In NICAM16-S, the conventional orographic gravity wave drag scheme (McFarlane, 1987) is tested to better simulate the location and strength of the subtropical jet. The wave generation parameter (α), which is proportional to the product of wave generation efficiency and representative horizontal wavenumber (Eq. 3.1b in McFarlane 1987), is roughly doubled as the horizontal mesh size is halved. Specifically, α is set to 3.38×10^{-5} for 56 km mesh, 7.12×10^{-5} for 28 km mesh, and 1.46×10^{-4} for 14 km mesh, respectively. Figure 12 and Figure 13 show the zonal mean zonal wind in boreal summer and winter, simulated with and without the gravity wave drag scheme. The zonal mean zonal wind simulated without the gravity wave drag scheme is biased poleward in both 56 km and 14 km mesh runs. The gravity wave drag scheme decelerates the zonal mean zonal wind at the poleward flank of the subtropical jet, especially in NH winter, reducing the locational bias of the jet. The impact of the gravity wave drag is larger in the 56 km mesh model than that in the 14 km mesh model. The pattern of the response of the zonal mean zonal wind to the orographic gravity wave drag scheme is similar to that of previous studies (e.g., Iwasaki et al., 1989; McFarlane, 1987).

Although it is believed that even a 14 km mesh is insufficient to explicitly simulate the effects of the orographic gravity wave drag on the mean field (Nappo, 2012), it may not be a wise choice to introduce such a gravity wave drag scheme to the global non-hydrostatic model. Gravity wave drag scheme introduces the uncertain parameter α, which is tuned to best simulate the climatology of the zonal wind for each resolution, although we did not tune α for each resolution. There is no solid guideline to determine α, including the dependency of the wave generation efficiency and representative horizontal wavenumber on the horizontal and vertical resolutions. Therefore, the use of a gravity wave drag scheme may hinder the pure resolution dependency of the mean field and suppress the advantages of the high-resolution model for simulating large-scale circulation in a seamless manner. Nevertheless, we determined to use the orographic gravity wave drag scheme for CMIP6 to reduce the locational bias of the subtropical jet so that an improvement of the tropical cyclone track would ensue. It is important to recognize the merits and demerits involved in the use of a gravity wave drag scheme and reconsider its use depending on the main purpose of the simulation.

4. Preliminary evaluations with observations including dependency of horizontal resolution

Table 6 shows the summary of the comparisons between NICAM16-S simulations and the observations along with a dependency of horizontal resolution. In terms of the global mean energy budget of the atmosphere, most of the bias features are similar to the previous NICAM climate simulations with 14 km mesh (Kodama et al., 2015), meaning that both OLR and OSR are underestimated. In the past, a high cloud amount was overestimated in the NICAM simulations. Now, a high cloud amount is comparable with the ISCCP observation in terms of global mean, although higher altitudes and thinner optical depth (not shown) are simulated, leading to the underestimation of OLR. Global mean precipitation and OLR are decreased as the resolution is increased, consistent with a previous study using 3.5–14 km mesh NICAM (Miyakawa and Miura, 2019). Low-level cloud amount is substantially underestimated, especially in the NICAM-7S and NICAM-8S runs, leading to the underestimation of OSR. Surface air temperature is slightly decreased as the resolution is increased in association with an increase in total cloud fraction. The most noticeable change from the previous simulation in terms of the global mean is the IWP. As described in Section 3.1, IWP is drastically increased by the update of cloud microphysics scheme.

5. Computational aspects

5.1 Simulations

Table 9 shows the elapsed time and the file size of the simulations by NICAM16-7S, NICAM16-8S and NICAM16-9S on the Earth Simulator 3 (NEC SX-ACE). File staging option was used in the NICAM16-8S and NICAM16-9S simulations, whereas the file was directly read from the global file system in the NICAM16-7S simulation to save time for queuing. The actual wall clock time, including queuing time, was a few times greater than SYPD in Table 9 for NICAM16-8S and NICAM16-9S depending on the congestion of the Earth Simulator 3. For the product run of NICAM16-8S, 160 nodes are used to finish a 101 year simulation within a realistic time.

Figure 14 breaks down the total elapsed time into each component of the model. Unlike a previous evaluation using the K computer (Yashiro et al., 2016), the measurement included an initial setup and input/output processes. Physics is a major part that contributes to the total elapsed time. Among the several physics components, the radiation scheme primarily contributes to the total elapsed time, followed by the cloud microphysics scheme, consistent with Yashiro et al. (2016) on the K computer. As the resolution increases, the percentage of the dynamics is increased and that of the cloud microphysics and near-surface processes decreases because time interval of the cloud microphysics and near-surface processes is set to be invariant throughout the models with different resolutions. Because the dynamics involves communication at every time step, some parts of the elapsed time counted as the dynamics can actually be waiting time because of node imbalance occurring in other processes.

5.2 Post-processes

The data are output in an icosahedral grid on the height above sea level (ASL) or on the standard pressure. The vertical interpolation from terrain-following height to the ASL height or standard pressure is performed online using second-order

5   Lagrange interpolation during the simulation.

Post-processes are performed in the following order: *ico2ll*, *roughen*, and *z2pre*.

(1) *ico2ll*

All the native icosahedral grid data are converted to high-resolution latitude–longitude grid data by area–weight averaging.

10   The interval of latitude and longitude is determined so that the longitudinal interval is close to the average interval of the icosahedral grid (Satoh et al., 2014) on the equator. Specifically, the interval of longitude and latitude is 0.56° for NICAM16-7S, 0.28° for NICAM16-8S, and 0.14° for NICAM16-9S.

(2) *roughen*

The high-resolution latitude–longitude grid data are coarsened to low-resolution latitude–longitude grid data by area–weight

15   averaging. It is often necessary to reduce the data size by coarsening, although CMIP6 does not request us to coarsen the data. We prepare 1.0°, 1.25°, and 2.5° data for analysis.

(3) *z2pre*

Several three-dimensional variables are converted from the ASL height to the standard pressure at this point by linear interpolation, if it is necessary.

After (1)–(3), monthly mean data are created.

Pressure velocity is diagnosed from the vertical velocity and temperature after *ico2ll*, assuming hydrostatic balance. Geopotential height is calculated from the linear interpolation of vertical levels using logarithms of pressure, assuming

25   constant gravity acceleration irrespective of height, which is a consistent treatment with the model configuration.

6. Summary

This paper described the experimental design, model description and impacts of the model updates on simulated climatology using NICAM prepared for CMIP6 HighResMIP (NICAM16-S). The major updates and their impacts are summarized as

30   follows:

- Update of the cloud microphysics scheme: Snow and cloud ice increase in the atmosphere, leading to less high cloud amount and more OLR.

- Implementation of the coupling between cloud microphysics and radiation schemes: The negative OLR bias is reduced in association with the larger cloud ice effective radius.

5 - Update of treatment of natural and anthropogenic aerosols: Local surface radiation budget is improved, especially over Africa and South Asia.

- Update of land model: Overall, the soil moisture and the precipitation increase and the surface air temperature decreases over the continent.

- Revision of the surface albedo values: Cold bias in the Greenland, the Himalayas and the Antarctic is reduced.

10 - Change in the diagnostics of ICE: Warm bias over the Arctic region is reduced.

- Introduction of the orographic gravity wave drag scheme: The location and strength of the zonal mean jet are improved.

Comprehensive evaluations and future projection using full HighResMIP data by NICAM16-S will be presented in a forthcoming paper.

15 **Code and data availability**

The exact model source code, input data or scripts to generate them, and scripts for the simulations and the post-processes used to produce the results presented in this paper are archived on Zenodo (doi:10.5281/zenodo.3727329). The model source codes are shared by the NICAM community and available for those who are interested as long as a user follows the terms and conditions described in http://www.nicam.jp/hiki/?Research+Collaborations. Most of the input data are freely accessible

20 from input4MIPs (https://esgf-node.llnl.gov/projects/input4mips/) for ocean boundary condition, GHG concentration, ozone and solar forcing, from ECMWF website (https://apps.ecmwf.int/datasets/data/era20c-daily/) for ERA-20C reanalysis, from supplemental materials of MACv2-SP description papers (Fiedler et al., 2019; Stevens et al., 2017) for anthropogenic aerosol data, and from U.S. Geological Survey website (https://doi.org/10.5066/F7DF6PQS) for GTOPO30 data. The other input data, obtained from ftp://iacftp.ethz.ch/pub_read/luo/CMIP6/MIROC3.2_29/ for volcanic aerosol and from

25 https://lpdaac.usgs.gov/ for leaf area index, are available on request from the corresponding author. HighResMIP Tier 1 (3) simulation data are (and will be) distributed freely through the Earth System Grid Federation (ESGF). Data on a series of sensitivity experiments are available on request from the corresponding author.

Author contributions

CK and ATN managed overall CMIP6 activity in NICAM group and prepared the initial and boundary conditions, and MS managed development and scientific activity in NICAM group. CK added interfaces of the initial and boundary conditions to NICAM, and TO added a function to output variables requested by CMIP6 and converted the output data using CMOR3. CK,

5 TO, TS, HY, MN, YY contributed to the development of NICAM16-S including bug fixes, and WS, TN, DG provided their schemes and parameters for the development. CK performed the product runs and all the sensitivity experiments described here, transferred the data to ESGF, and wrote a major part of this paper. TS wrote most part of Section 3.1 and 3.2 and TS, ATN, DG, HM, TN modified the manuscript. All the authors provided advice for the development of NICAM16-S and/or experimental design and reviewed the manuscript.

Competing interests

The authors declare that they have no conflict of interest.

Acknowledgment

15 The authors would like to thank Hiroaki Tatebe and Ryosuke Shibuya for discussion on model configurations and Manabu Abe and Takahiro Inoue for technical advice for CMIP6. CERES, CloudSat, ISCCP, and GPCP data are obtained from the National Aeronautics and Space Administration (NASA), JRA-55 data from the JMA, and GridSat data from the National Oceanic and Atmospheric Administration (NOAA). This study was supported by the Environment Research and Technology Development Fund (2RF-1701) of the Environmental Restoration and Conservation Agency of Japan (ERCA) and the

20 Integrated Research Program for Advancing Climate Models (TOUGOU) and the FLAGSHIP2020 project within the priority study4, of the Ministry of Education, Culture, Sports, Science and Technology (MEXT) of Japan. The HighResMIP simulations and most of the sensitivity experiments were performed on the Earth Simulator at the Japan Agency for Marine-Earth Science and Technology (JAMSTEC), and some of them on the K computer (proposal number hp150287, hp160230, hp170234, hp180182, and hp190152).

References

Adler, R. F., Huffman, G. J., Chang, A., Ferraro, R., Xie, P.-P., Janowiak, J., Rudolf, B., Schneider, U., Curtis, S., Bolvin, D., Gruber, A., Susskind, J., Arkin, P. and Nelkin, E.: The version-2 global precipitation climatology project (GPCP) monthly precipitation analysis (1979–present), J. Hydrometeorol., 4(6), 1147–1167, doi:10.1175/1525-
5   7541(2003)004<1147:TVGPCP>2.0.CO;2, 2003.

Aoki, T., Kuchiki, K., Niwano, M., Kodama, Y., Hosaka, M. and Tanaka, T.: Physically based snow albedo model for calculating broadband albedos and the solar heating profile in snowpack for general circulation models, J. Geophys. Res., 116(D11), D11114, doi:10.1029/2010JD015507, 2011.

Armstrong, R. L. and and Brun, E., Eds.: Snow and Climate: Physical Processes, Surface Energy Exchange and Modeling,
10   Cambridge Univ. Press, Cambridge, U. K., 2008.

Austin, R. T. and Stephens, G. L.: Retrieval of stratus cloud microphysical parameters using millimeter-wave radar and visible optical depth in preparation for CloudSat: 1. Algorithm formulation, J. Geophys. Res. Atmos., 106(D22), 28233–28242, doi:10.1029/2000JD000293, 2001.

Austin, R. T., Heymsfield, A. J. and Stephens, G. L.: Retrieval of ice cloud microphysical parameters using the CloudSat
15   millimeter-wave radar and temperature, J. Geophys. Res., 114, D00A23, doi:10.1029/2008JD010049, 2009.

Bodas-Salcedo, A., Webb, M. J., Brooks, M. E., Ringer, M. A., Williams, K. D., Milton, S. F. and Wilson, D. R.: Evaluating cloud systems in the Met Office global forecast model using simulated CloudSat radar reflectivities, J. Geophys. Res., 113, D00A13, doi:10.1029/2007JD009620, 2008.

Bodas-Salcedo, A., Webb, M. J., Bony, S., Chepfer, H., Dufresne, J. L., Klein, S. A., Zhang, Y., Marchand, R., Haynes, J.
20   M., Pincus, R. and John, V. O.: {COSP} Satellite simulation software for model assessment, Bull. Amer. Meteor. Soc., 92(8), 1023–1043, doi:10.1175/2011BAMS2856.1, 2011.

Chen, Y.-W., Seiki, T., Kodama, C., Satoh, M., Noda, A. T. and Yamada, Y.: High Cloud Responses to Global Warming Simulated by Two Different Cloud Microphysics Schemes Implemented in the Nonhydrostatic Icosahedral Atmospheric Model (NICAM), J. Clim., 29(16), 5949–5964, doi:10.1175/JCLI-D-15-0668.1, 2016.

25   Chen, Y.-W., Seiki, T., Kodama, C., Satoh, M. and Noda, A. T.: Impact of precipitating ice hydrometeors on longwave radiative effect estimated by a global cloud-system resolving model, J. Adv. Model. Earth Syst., 10(2), 284–296, doi:10.1002/2017MS001180, 2018.

Chepfer, H., Bony, S., Winker, D., Chiriaco, M., Dufresne, J. L. and Seze, G.: Use of {CALIPSO} lidar observations to evaluate the cloudiness simulated by a climate model, Geophys. Res. Lett., 35(15), L15704, doi:10.1029/2008GL034207,
30   2008.

Fairall, C. W., Bradley, E. F., Hare, J. E., Grachev, A. A. and Edson, J. B.: Bulk Parameterization of Air–Sea Fluxes: Updates and Verification for the COARE Algorithm, J. Clim., 16(4), 571–591, doi:10.1175/1520-0442(2003)016<0571:BPOASF>2.0.CO;2, 2003.

Fiedler, S., Stevens, B., Gidden, M., Smith, S. J., Riahi, K. and van Vuuren, D.: First forcing estimates from the future CMIP6 scenarios of anthropogenic aerosol optical properties and an associated Twomey effect, Geosci. Model Dev., 12(3), 989–1007, doi:10.5194/gmd-12-989-2019, 2019.

Field, P. R., Hogan, R. J., Brown, P. R. A., Illingworth, A. J., Choularton, T. W. and Cotton, R. J.: Parametrization of ice-
5   particle size distributions for mid-latitude stratiform cloud, Q. J. R. Meteorol. Soc., 131(609), 1997–2017, doi:10.1256/qj.04.134, 2005.

Fu, Q.: An Accurate Parameterization of the Solar Radiative Properties of Cirrus Clouds for Climate Models, J. Clim., 9(9), 2058–2082, doi:10.1175/1520-0442(1996)009<2058:AAPOTS>2.0.CO;2, 1996.

Fu, Q., Yang, P. and Sun, W. B.: An Accurate Parameterization of the Infrared Radiative Properties of Cirrus Clouds for
10 Climate Models, J. Clim., 11(9), 2223–2237, doi:10.1175/1520-0442(1998)011<2223:AAPOTI>2.0.CO;2, 1998.

Fukutomi, Y., Kodama, C., Yamada, Y., Noda, A. T. and Satoh, M.: Tropical synoptic-scale wave disturbances over the western Pacific simulated by a global cloud-system resolving model, Theor. Appl. Climatol., 124(3–4), 737–755, doi:10.1007/s00704-015-1456-4, 2016.

Gilmore, M. S., Straka, J. M. and Rasmussen, E. N.: Precipitation Uncertainty Due to Variations in Precipitation Particle
15 Parameters within a Simple Microphysics Scheme, Mon. Weather Rev., 132(11), 2610–2627, doi:10.1175/MWR2810.1, 2004.

Goto, D., Takemura, T. and Nakajima, T.: Importance of global aerosol modeling including secondary organic aerosol formed from monoterpene, J. Geophys. Res., 113(D7), D07205, doi:10.1029/2007JD009019, 2008.

Goto, D., Nakajima, T., Takemura, T. and Sudo, K.: A study of uncertainties in the sulfate distribution and its radiative
20 forcing associated with sulfur chemistry in a global aerosol model, Atmos. Chem. Phys., 11(21), 10889–10910, doi:10.5194/acp-11-10889-2011, 2011.

Goto, D., Nakajima, T., Tie, D., Yashiro, H., Sato, Y., Suzuki, K., Uchida, J., Misawa, S., Yonemoto, R., Trieu, T. T. N., Tomita, H. and Satoh, M.: Multi-scale Simulations of Atmospheric Pollutants Using a Non-hydrostatic Icosahedral Atmospheric Model, in Land-Atmospheric Research Applications in South and Southeast Asia, edited by K. Vadrevu, T.
25 Ohara, and C. Justice, pp. 277–302, Springer International Publishing., 2018.

Grabowski, W. W.: Impact of explicit atmosphere–ocean coupling on MJO-like coherent structures in idealized aquaplanet simulations, J. Atmos. Sci., 63(9), 2289–2306, doi:10.1175/JAS3740.1, 2006.

Haarsma, R. J., Roberts, M. J., Vidale, P. L., Senior, C. A., Bellucci, A., Bao, Q., Chang, P., Corti, S., Fučkar, N. S., Guemas, V., von Hardenberg, J., Hazeleger, W., Kodama, C., Koenigk, T., Leung, L. R. R., Lu, J., Luo, J.-J., Mao, J., Mizielinski, M.
30 S., Mizuta, R., Nobre, P., Satoh, M., Scoccimarro, E., Semmler, T., Small, J. and von Storch, J.-S.: High Resolution Model Intercomparison Project (HighResMIP v1.0) for CMIP6, Geosci. Model Dev., 9(11), 4185–4208, doi:10.5194/gmd-9-4185-2016, 2016.

Hashino, T., Satoh, M., Hagihara, Y., Kubota, T., Matsui, T., Nasuno, T. and Okamoto, H.: Evaluating cloud microphysics from NICAM against CloudSat and CALIPSO, J. Geophys. Res. Atmos., 118(13), 7273–7292, doi:10.1002/jgrd.50564, 2013.

Hashino, T., Satoh, M., Hagihara, Y., Kato, S., Kubota, T., Matsui, T., Nasuno, T., Okamoto, H. and Sekiguchi, M.: Evaluating Arctic cloud radiative effects simulated by NICAM with A-train, J. Geophys. Res. Atmos., 121(12), 7041–7063, doi:10.1002/2016JD024775, 2016.

Haynes, J. M., Marchand, R. T., Luo, Z., Bodas-Salcedo, A. and Stephens, G. L.: A multipurpose radar simulation package:
5 {QuickBeam}, Bull. Amer. Meteor. Soc., 88(11), 1723–1727, doi:10.1175/BAMS-88-11-1723, 2007.

Hegglin, M., Kinnison, D., Lamarque, J.-F. and Plummer, D.: CCMI ozone in support of CMIP6 - version 1.0. Version 20160711., 2016.

Hegglin, M., Kinnison, D., Lamarque, J.-F. and Plummer, D.: input4MIPs.CMIP6.ScenarioMIP.UReading.UReading-CCMI-ssp585-1-0, Version 20181101., 2018.

10 Hegglin, M., Kinnison, D., Plummer, D. and Al., E.: Historical and future ozone database (1850-2100) in support of CMIP6, Geosci. Model Dev., n.d.

Heymsfield, A. J. and Donner, L. J.: A Scheme for Parameterizing Ice-Cloud Water Content in General Circulation Models, J. Atmos. Sci., 47(15), 1865–1877, doi:10.1175/1520-0469(1990)047<1865:ASFPIC>2.0.CO;2, 1990.

Hong, S.-Y., Dudhia, J. and Chen, S.-H.: A Revised Approach to Ice Microphysical Processes for the Bulk Parameterization
15 of Clouds and Precipitation, Mon. Weather Rev., 132(1), 103–120, doi:10.1175/1520-0493(2004)132<0103:ARATIM>2.0.CO;2, 2004.

Iwasaki, T., Yamada, S. and Tada, K.: A parameterization scheme of orographic gravity wave drag with two different vertical partitionings {Part I}: Impacts on medium-range forecasts, J. Meteor. Soc. Japan, 67(1), 11–27, 1989.

Kato, S., Rose, F. G., Rutan, D. A., Thorsen, T. J., Loeb, N. G., Doelling, D. R., Huang, X., Smith, W. L., Su, W. and Ham,
20 S.-H.: Surface Irradiances of Edition 4.0 Clouds and the Earth's Radiant Energy System (CERES) Energy Balanced and Filled (EBAF) Data Product, J. Clim., 31(11), 4501–4527, doi:10.1175/JCLI-D-17-0523.1, 2018.

Kennedy, J., Titchner, H., Rayner, N. and Roberts, M.: input4MIPs.MOHC.SSTsAndSeaIce.HighResMIP.MOHC-HadISST-2-2-0-0-0, Version 20170201, Earth System Grid Federation., 2017.

Kennedy, J., Titchner, H., Rayner, N. and Roberts, M.: input4MIPs.CMIP6.HighResMIP.MOHC.MOHC-highresSST-
25 future-1-0-1, Version 20190215., 2019.

Kikuchi, K., Kodama, C., Nasuno, T., Nakano, M., Miura, H., Satoh, M., Noda, A. T. and Yamada, Y.: Tropical intraseasonal oscillation simulated in an AMIP-type experiment by NICAM, Clim. Dyn., 48(7–8), 2507–2528, doi:10.1007/s00382-016-3219-z, 2017.

Kilpatrick, T., Xie, S.-P. and Nasuno, T.: Diurnal convection-wind coupling in the Bay of Bengal, J. Geophys. Res. Atmos.,
30 122(18), 9705–9720, doi:10.1002/2017JD027271, 2017.

Kinter, J. L., Cash, B., Achuthavarier, D., Adams, J., Altshuler, E., Dirmeyer, P., Doty, B., Huang, B., Jin, E. K. K., Marx, L., Manganello, J., Stan, C., Wakefield, T., Palmer, T., Hamrud, M., Jung, T., Miller, M., Towers, P., Wedi, N., Satoh, M., Tomita, H., Kodama, C., Nasuno, T., Oouchi, K., Yamada, Y., Taniguchi, H., Andrews, P., Baer, T., Ezell, M., Halloy, C.,

John, D., Loftis, B., Mohr, R. and Wong, K.: Revolutionizing Climate Modeling with Project Athena: A Multi-Institutional, International Collaboration, Bull. Am. Meteorol. Soc., 94(2), 231–245, doi:10.1175/BAMS-D-11-00043.1, 2013.

Knapp, K. R., Ansari, S., Bain, C. L., Bourassa, M. A., Dickinson, M. J., Funk, C., Helms, C. N., Hennon, C. C., Holmes, C. D., Huffman, G. J., Kossin, J. P., Lee, H.-T., Loew, A. and Magnusdottir, G.: Globally Gridded Satellite Observations for

5 Climate Studies, Bull. Am. Meteorol. Soc., 92(7), 893–907, doi:10.1175/2011BAMS3039.1, 2011.

Knight, C. A., Cooper, W. A., Breed, D. W., Paluch, I. R., Smith, P. L. and Vali, G.: Microphysics, in Hailstorms of the Central High Plains, edited by C. Knight and P. Squires, pp. 151–193, Colorado Associated University Press. [online] Available from: https://opensky.ucar.edu/islandora/object/books%3A140, 1982.

Kobayashi, S., Ota, Y., Harada, Y., Ebita, A., Moriya, M., Onoda, H., Onogi, K., Kamahori, H., Kobayashi, C., Endo, H.,

10 Miyaoka, K. and Takahashi, K.: The JRA-55 reanalysis: general specifications and basic characteristics, J. Meteorol. Soc. Japan. Ser. II, 93(1), 5–48, doi:10.2151/jmsj.2015-001, 2015.

Kodama, C., Noda, A. T. T. and Satoh, M.: An assessment of the cloud signals simulated by NICAM using ISCCP, CALIPSO, and CloudSat satellite simulators, J. Geophys. Res. Atmos., 117(D12), n/a-n/a, doi:10.1029/2011JD017317, 2012.

Kodama, C., Yamada, Y., Noda, A. T., Kikuchi, K., Kajikawa, Y., Nasuno, T., Tomita, T., Yamaura, T., Takahashi, H. G.,

15 Hara, M., Kawatani, Y., Satoh, M., Sugi, M. and Satoh, M.: A 20-year climatology of a NICAM AMIP-type simulation, J. Meteorol. Soc. Japan. Ser. II, 93(4), 393–424, doi:10.2151/jmsj.2015-024, 2015.

Kodama, C., Stevens, B., Mauritsen, T., Seiki, T. and Satoh, M.: A New Perspective for Future Precipitation Change from Intense Extratropical Cyclones, Geophys. Res. Lett., 46(21), 12435–12444, doi:10.1029/2019GL084001, 2019.

Lang, S., Tao, W.-K., Simpson, J., Cifelli, R., Rutledge, S., Olson, W. and Halverson, J.: Improving Simulations of

20 Convective Systems from TRMM LBA: Easterly and Westerly Regimes, J. Atmos. Sci., 64(4), 1141–1164, doi:10.1175/JAS3879.1, 2007.

Li, J.-L. F., Forbes, R. M., Waliser, D. E., Stephens, G. and Lee, S.: Characterizing the radiative impacts of precipitating snow in the ECMWF Integrated Forecast System global model, J. Geophys. Res. Atmos., 119(16), 9626–9637, doi:10.1002/2014JD021450, 2014.

25 Li, J.-L. F., Lee, W.-L., Waliser, D., Wang, Y.-H., Yu, J.-Y., Jiang, X., L'Ecuyer, T., Chen, Y.-C., Kubar, T., Fetzer, E. and Mahakur, M.: Considering the radiative effects of snow on tropical Pacific Ocean radiative heating profiles in contemporary GCMs using A-Train observations, J. Geophys. Res. Atmos., 121(4), 1621–1636, doi:10.1002/2015JD023587, 2016.

Lin, Y.-L., Farley, R. D. and Orville, H. D.: Bulk Parameterization of the Snow Field in a Cloud Model, J. Clim. Appl. Meteorol., 22(6), 1065–1092, doi:10.1175/1520-0450(1983)022<1065:BPOTSF>2.0.CO;2, 1983.

30 Loeb, N. G., Doelling, D. R., Wang, H., Su, W., Nguyen, C., Corbett, J. G., Liang, L., Mitrescu, C., Rose, F. G. and Kato, S.: Clouds and the Earth's Radiant Energy System (CERES) Energy Balanced and Filled (EBAF) Top-of-Atmosphere (TOA) Edition-4.0 Data Product, J. Clim., 31(2), 895–918, doi:10.1175/JCLI-D-17-0208.1, 2018.

Louis, J.-F.: A parametric model of vertical eddy fluxes in the atmosphere, Boundary-Layer Meteorol., 17(2), 187–202, doi:10.1007/BF00117978, 1979.

Mahowald, N., Albani, S., Kok, J. F., Engelstaeder, S., Scanza, R., Ward, D. S. and Flanner, M. G.: The size distribution of desert dust aerosols and its impact on the Earth system, Aeolian Res., 15, 53–71, doi:10.1016/j.aeolia.2013.09.002, 2014.

Masunaga, H., Matsui, T., Tao, W., Hou, A. Y., Kummerow, C. D., Nakajima, T., Bauer, P., Olson, W. S., Sekiguchi, M. and Nakajima, T. Y.: Satellite Data Simulator Unit, Bull. Am. Meteorol. Soc., 91(12), 1625–1632,

5   doi:10.1175/2010BAMS2809.1, 2010.

Matsui, T., Zeng, X., Tao, W.-K., Masunaga, H., Olson, W. S. and Lang, S.: Evaluation of Long-Term Cloud-Resolving Model Simulations Using Satellite Radiance Observations and Multifrequency Satellite Simulators, J. Atmos. Ocean. Technol., 26(7), 1261–1274, doi:10.1175/2008JTECHA1168.1, 2009.

Matsuoka, D., Nakano, M., Sugiyama, D. and Uchida, S.: Deep learning approach for detecting tropical cyclones and their

10   precursors in the simulation by a cloud-resolving global nonhydrostatic atmospheric model, Prog. Earth Planet. Sci., 5(1), 80, doi:10.1186/s40645-018-0245-y, 2018.

Matthes, K., Funke, B., Kruschke, T. and Wahl, S.: input4MIPs.SOLARIS-HEPPA.solar.CMIP.SOLARIS-HEPPA-3-2. Version 20170103., 2017a.

Matthes, K., Funke, B., Andersson, M. E., Barnard, L., Beer, J., Charbonneau, P., Clilverd, M. A., Dudok de Wit, T.,

15   Haberreiter, M., Hendry, A., Jackman, C. H., Kretzschmar, M., Kruschke, T., Kunze, M., Langematz, U., Marsh, D. R., Maycock, A. C., Misios, S., Rodger, C. J., Scaife, A. A., Seppälä, A., Shangguan, M., Sinnhuber, M., Tourpali, K., Usoskin, I., van de Kamp, M., Verronen, P. T. and Versick, S.: Solar forcing for CMIP6 (v3.2), Geosci. Model Dev., 10(6), 2247–2302, doi:10.5194/gmd-10-2247-2017, 2017b.

McCoy, D. T., Field, P. R., Elsaesser, G. S., Bodas-Salcedo, A., Kahn, B. H., Zelinka, M. D., Kodama, C., Mauritsen, T.,

20   Vanniere, B., Roberts, M., Vidale, P. L., Saint-Martin, D., Voldoire, A., Haarsma, R., Hill, A., Shipway, B. and Wilkinson, J.: Cloud feedbacks in extratropical cyclones: insight from long-term satellite data and high-resolution global simulations, Atmos. Chem. Phys., 19(2), 1147–1172, doi:10.5194/acp-19-1147-2019, 2019.

McFarlane, N. A.: The effect of orographically excited gravity wave drag on the general circulation of the lower stratosphere and troposphere, J. Atmos. Sci., 44(14), 1775–1800, doi:10.1175/1520-0469(1987)044<1775:TEOOEG>2.0.CO;2, 1987.

25   McFarlane, N. A., Boer, G. J., Blanchet, J.-P. and Lazare, M.: The Canadian Climate Centre Second-Generation General Circulation Model and Its Equilibrium Climate, J. Clim., 5(10), 1013–1044, doi:10.1175/1520-0442(1992)005<1013:TCCCSG>2.0.CO;2, 1992.

Meinshausen, M. and Nicholls, Z. R. J.: UoM-REMIND-MAGPIE-ssp585-1-2-1 GHG concentrations. Version 20181127., 2018.

30   Meinshausen, M. and Vogel, E.: input4MIPs.UoM.GHGConcentrations.CMIP.UoM-CMIP-1-2-0. Version 20160830., 2016.

Meinshausen, M., Vogel, E., Nauels, A., Lorbacher, K., Meinshausen, N., Etheridge, D. M., Fraser, P. J., Montzka, S. A., Rayner, P. J., Trudinger, C. M., Krummel, P. B., Beyerle, U., Canadell, J. G., Daniel, J. S., Enting, I. G., Law, R. M., Lunder, C. R., O'Doherty, S., Prinn, R. G., Reimann, S., Rubino, M., Velders, G. J. M., Vollmer, M. K., Wang, R. H. J.

and Weiss, R.: Historical greenhouse gas concentrations for climate modelling (CMIP6), Geosci. Model Dev., 10(5), 2057–2116, doi:10.5194/gmd-10-2057-2017, 2017.

Michibata, T., Suzuki, K., Sekiguchi, M. and Takemura, T.: Prognostic Precipitation in the MIROC6-SPRINTARS GCM: Description and Evaluation Against Satellite Observations, J. Adv. Model. Earth Syst., 11(3), 839–860,

5 doi:10.1029/2018MS001596, 2019.

Mitchell, D. L.: Use of Mass- and Area-Dimensional Power Laws for Determining Precipitation Particle Terminal Velocities, J. Atmos. Sci., 53(12), 1710–1723, doi:10.1175/1520-0469(1996)053<1710:UOMAAD>2.0.CO;2, 1996.

Miyakawa, T. and Miura, H.: Resolution Dependencies of Tropical Convection in a Global Cloud/Cloud-System Resolving Model, J. Meteorol. Soc. Japan. Ser. II, 97(3), 745–756, doi:10.2151/jmsj.2019-034, 2019.

10 Moon, I.-J., Ginis, I., Hara, T. and Thomas, B.: A Physics-Based Parameterization of Air–Sea Momentum Flux at High Wind Speeds and Its Impact on Hurricane Intensity Predictions, Mon. Weather Rev., 135(8), 2869–2878, doi:10.1175/MWR3432.1, 2007.

Na, Y., Fu, Q. and Kodama, C.: Precipitation Probability and Its Future Changes From a Global Cloud-Resolving Model and CMIP6 Simulations, J. Geophys. Res. Atmos., 125(5), doi:10.1029/2019JD031926, 2020.

15 Nakajima, T., Tsukamoto, M., Tsushima, Y., Numaguti, A. and Kimura, T.: Modeling of the radiative process in an atmospheric general circulation model, Appl. Opt., 39(39), 4869–4878, 2000.

Nakanishi, M. and Niino, H.: An improved Mellor–Yamada level-3 model: Its numerical stability and application to a regional prediction of advection fog, Boundary-Layer Meteorol., 119(2), 397–407, doi:10.1007/s10546-005-9030-8, 2006.

Nakano, M. and Kikuchi, K.: Seasonality of Intraseasonal Variability in Global Climate Models, Geophys. Res. Lett., 46(8),

20 4441–4449, doi:10.1029/2019GL082443, 2019.

Nappo, C.: An Introduction to Atmospheric Gravity Waves, 2nd ed., Academic Press., 2012.

Nitta, T., Yoshimura, K. and Abe-Ouchi, A.: Impact of Arctic Wetlands on the Climate System: Model Sensitivity Simulations with the MIROC5 AGCM and a Snow-Fed Wetland Scheme, J. Hydrometeorol., 18(11), 2923–2936, doi:10.1175/JHM-D-16-0105.1, 2017.

25 Niwano, M., Aoki, T., Kuchiki, K., Hosaka, M., Kodama, Y., Yamaguchi, S., Moytoyoshi, H. and Iwata, Y.: Evaluation of updated physical snowpack model SMAP, Bull. Glaciol. Res., 32, 65–78, doi:10.5331/bgr.32.65, 2014.

Noda, A. T., Oouchi, K., Satoh, M., Tomita, H., Iga, S. and Tsushima, Y.: Importance of the subgrid-scale turbulent moist process: Cloud distribution in global cloud-resolving simulations, Atmos. Res., 96(2–3), 208–217, doi:10.1016/j.atmosres.2009.05.007, 2010.

30 Noda, A. T., Seiki, T., Satoh, M. and Yamada, Y.: High cloud size dependency in the applicability of the fixed anvil temperature hypothesis using global nonhydrostatic simulations, Geophys. Res. Lett., doi:10.1002/2016GL067742, 2016.

Noda, A. T., Kodama, C., Yamada, Y., Satoh, M., Ogura, T. and Ohno, T.: Responses of Clouds and Large-Scale Circulation to Global Warming Evaluated From Multidecadal Simulations Using a Global Nonhydrostatic Model, J. Adv. Model. Earth Syst., 11(9), 2980–2995, doi:10.1029/2019MS001658, 2019.

O'Neill, B. C., Tebaldi, C., van Vuuren, D. P., Eyring, V., Friedlingstein, P., Hurtt, G., Knutti, R., Kriegler, E., Lamarque, J.-F., Lowe, J., Meehl, G. A., Moss, R., Riahi, K. and Sanderson, B. M.: The Scenario Model Intercomparison Project (ScenarioMIP) for CMIP6, Geosci. Model Dev., 9(9), 3461–3482, doi:10.5194/gmd-9-3461-2016, 2016.

Omar, A. H.: Development of global aerosol models using cluster analysis of Aerosol Robotic Network (AERONET)

5   measurements, J. Geophys. Res., 110(D10), D10S14, doi:10.1029/2004JD004874, 2005.

Poli, P., Hersbach, H., Dee, D. P., Berrisford, P., Simmons, A. J., Vitart, F., Laloyaux, P., Tan, D. G. H., Peubey, C., Thépaut, J.-N., Trémolet, Y., Hólm, E. V., Bonavita, M., Isaksen, L. and Fisher, M.: ERA-20C: An Atmospheric Reanalysis of the Twentieth Century, J. Clim., 29(11), 4083–4097, doi:10.1175/JCLI-D-15-0556.1, 2016.

Roberts, M. J., Vidale, P. L., Senior, C., Hewitt, H. T., Bates, C., Berthou, S., Chang, P., Christensen, H. M., Danilov, S.,

10   Demory, M.-E., Griffies, S. M., Haarsma, R., Jung, T., Martin, G., Minobe, S., Ringler, T., Satoh, M., Schiemann, R., Scoccimarro, E., Stephens, G. and Wehner, M. F.: The Benefits of Global High Resolution for Climate Simulation: Process Understanding and the Enabling of Stakeholder Decisions at the Regional Scale, Bull. Am. Meteorol. Soc., 99(11), 2341–2359, doi:10.1175/BAMS-D-15-00320.1, 2018.

Roh, W. and Satoh, M.: Evaluation of Precipitating Hydrometeor Parameterizations in a Single-Moment Bulk Microphysics

15   Scheme for Deep Convective Systems over the Tropical Central Pacific, J. Atmos. Sci., 71(7), 2654–2673, doi:10.1175/JAS-D-13-0252.1, 2014.

Roh, W. and Satoh, M.: Extension of a Multisensor Satellite Radiance-Based Evaluation for Cloud System Resolving Models, J. Meteorol. Soc. Japan. Ser. II, 96(1), 55–63, doi:10.2151/jmsj.2018-002, 2018.

Roh, W., Satoh, M. and Nasuno, T.: Improvement of a Cloud Microphysics Scheme for a Global Nonhydrostatic Model

20   Using TRMM and a Satellite Simulator, J. Atmos. Sci., 74(1), 167–184, doi:10.1175/JAS-D-16-0027.1, 2017.

Rossow, W. B. and Schiffer, R. A.: Advances in Understanding Clouds from ISCCP, Bull. Am. Meteorol. Soc., 80(11), 2261–2287, doi:10.1175/1520-0477(1999)080<2261:AIUCFI>2.0.CO;2, 1999.

Rutledge, S. A. and Hobbs, P. V.: The Mesoscale and Microscale Structure and Organization of Clouds and Precipitation in Midlatitude Cyclones. XII: A Diagnostic Modeling Study of Precipitation Development in Narrow Cold-Frontal Rainbands,

25   J. Atmos. Sci., 41(20), 2949–2972, doi:10.1175/1520-0469(1984)041<2949:TMAMSA>2.0.CO;2, 1984.

Satoh, M., Matsuno, T., Tomita, H., Miura, H., Nasuno, T. and Iga, S.: Nonhydrostatic icosahedral atmospheric model (NICAM) for global cloud resolving simulations, J. Comput. Phys., 227(7), 3486–3514, doi:10.1016/j.jcp.2007.02.006, 2008.

Satoh, M., Inoue, T. and Miura, H.: Evaluations of cloud properties of global and local cloud system resolving models using CALIPSO and CloudSat simulators, J. Geophys. Res., 115, D00H14, doi:10.1029/2009JD012247, 2010.

30   Satoh, M., Tomita, H., Yashiro, H., Miura, H., Kodama, C., Seiki, T., Noda, A. T., Yamada, Y., Goto, D., Sawada, M., Miyoshi, T., Niwa, Y., Hara, M., Ohno, T., Iga, S., Arakawa, T., Inoue, T. and Kubokawa, H.: The non-hydrostatic icosahedral atmospheric model: Description and development, Prog. Earth Planet. Sci., 1(1), 18, doi:10.1186/s40645-014-0018-1, 2014.

Satoh, M., Yamada, Y., Sugi, M., Kodama, C. and Noda, A. T. T.: Constraint on future change in global frequency of tropical cyclones due to global warming, J. Meteor. Soc. Japan, 93(4), 489–500, doi:10.2151/jmsj.2015-025, 2015.

Satoh, M., Noda, A. T., Seiki, T., Chen, Y.-W., Kodama, C., Yamada, Y., Kuba, N. and Sato, Y.: Toward reduction of the uncertainties in climate sensitivity due to cloud processes using a global non-hydrostatic atmospheric model, Prog. Earth

5 Planet. Sci., 5(1), 67, doi:10.1186/s40645-018-0226-1, 2018.

Satoh, M., Stevens, B., Judt, F., Khairoutdinov, M., Lin, S.-J., Putman, W. M. and Düben, P.: Global Cloud-Resolving Models, Curr. Clim. Chang. Reports, doi:10.1007/s40641-019-00131-0, 2019.

Seiki, T., Satoh, M., Tomita, H. and Nakajima, T.: Simultaneous evaluation of ice cloud microphysics and nonsphericity of the cloud optical properties using hydrometeor video sonde and radiometer sonde in situ observations, J. Geophys. Res.

10 Atmos., 119(11), 6681–6701, doi:10.1002/2013JD021086, 2014.

Seiki, T., Kodama, C., Noda, A. T. A. T. and Satoh, M.: Improvement in Global Cloud-System-Resolving Simulations by Using a Double-Moment Bulk Cloud Microphysics Scheme, J. Clim., 28(6), 2405–2419, doi:10.1175/JCLI-D-14-00241.1, 2015a.

Seiki, T., Kodama, C., Satoh, M., Hashino, T., Hagihara, Y. and Okamoto, H.: Vertical grid spacing necessary for simulating

15 tropical cirrus clouds with a high-resolution atmospheric general circulation model, Geophys. Res. Lett., 42(10), 4150–4157, doi:10.1002/2015GL064282, 2015b.

Sekiguchi, M. and Nakajima, T.: A k-distribution-based radiation code and its computational optimization for an atmospheric general circulation model, J. Quant. Spectrosc. Radiat. Transf., 109(17–18), 2779–2793, doi:10.1016/j.jqsrt.2008.07.013, 2008.

20 Shabanov, N. V., Dong Huang, Wenze Yang, Tan, B., Knyazikhin, Y., Myneni, R. B., Ahl, D. E., Gower, S. T., Huete, A. R., Aragao, L. E. O. C. and Shimabukuro, Y. E.: Analysis and optimization of the MODIS leaf area index algorithm retrievals over broadleaf forests, IEEE Trans. Geosci. Remote Sens., 43(8), 1855–1865, doi:10.1109/TGRS.2005.852477, 2005.

Shukla, J., Hagedorn, R., Hoskins, B., Kinter, J., Marotzke, J., Miller, M., Palmer, T. N. and Slingo, J.: Revolution in climate prediction is both necessary and possible a declaration at the world modelling summit for climate prediction, Bull. Amer.

25 Meteor. Soc., 90(2), 175–178, doi:10.1175/2008BAMS2759.1, 2009.

Stevens, B., Fiedler, S., Kinne, S., Peters, K., Rast, S., Müsse, J., Smith, S. J. and Mauritsen, T.: MACv2-SP: a parameterization of anthropogenic aerosol optical properties and an associated Twomey effect for use in CMIP6, Geosci. Model Dev., 10(1), 433–452, doi:10.5194/gmd-10-433-2017, 2017.

Sugi, M., Yamada, Y., Yoshida, K., Mizuta, R., Nakano, M., Kodama, C. and Satoh, M.: Future changes in the global

30 frequency of tropical cyclone seeds, Submitt. to SOLA, n.d.

Suzuki, K., Nakajima, T., Satoh, M., Tomita, H., Takemura, T., Nakajima, T. Y. and Stephens, G. L.: Global cloud-system-resolving simulation of aerosol effect on warm clouds, Geophys. Res. Lett., 35(19), L19817, doi:10.1029/2008GL035449, 2008.

Takahashi, H. G., Kamizawa, N., Nasuno, T., Yamada, Y., Kodama, C., Sugimoto, S. and Satoh, M.: Response of the Asian Summer Monsoon Precipitation to Global Warming in a High-Resolution Global Nonhydrostatic Model, J. Clim., n.d.

Takata, K., Emori, S. and Watanabe, T.: Development of the minimal advanced treatments of surface interaction and runoff, Glob. Planet. Change, 38(1–2), 209–222, doi:10.1016/S0921-8181(03)00030-4, 2003.

5   Takemura, T., Okamoto, H., Maruyama, Y., Numaguti, A., Higurashi, A. and Nakajima, T.: Global three-dimensional simulation of aerosol optical thickness distribution of various origins, J. Geophys. Res. Atmos., 105(D14), 17853–17873, doi:10.1029/2000JD900265, 2000.

Takemura, T., Nakajima, T., Dubovik, O., Holben, B. N. and Kinne, S.: Single-Scattering Albedo and Radiative Forcing of Various Aerosol Species with a Global Three-Dimensional Model, J. Clim., 15(4), 333–352, doi:10.1175/1520-

10   0442(2002)015<0333:SSAARF>2.0.CO;2, 2002.

Takemura, T., Nozawa, T., Emori, S., Nakajima, T. Y. and Nakajima, T.: Simulation of climate response to aerosol direct and indirect effects with aerosol transport-radiation model, J. Geophys. Res., 110(D2), D02202, doi:10.1029/2004JD005029, 2005.

Takemura, T., Egashira, M., Matsuzawa, K., Ichijo, H., O'ishi, R. and Abe-Ouchi, A.: A simulation of the global distribution

15   and radiative forcing of soil dust aerosols at the Last Glacial Maximum, Atmos. Chem. Phys., 9(9), 3061–3073, doi:10.5194/acp-9-3061-2009, 2009.

Tatebe, H., Ogura, T., Nitta, T., Komuro, Y., Ogochi, K., Takemura, T., Sudo, K., Sekiguchi, M., Abe, M., Saito, F., Chikira, M., Watanabe, S., Mori, M., Hirota, N., Kawatani, Y., Mochizuki, T., Yoshimura, K., Takata, K., O'ishi, R., Yamazaki, D., Suzuki, T., Kurogi, M., Kataoka, T., Watanabe, M. and Kimoto, M.: Description and basic evaluation of

20   simulated mean state, internal variability, and climate sensitivity in MIROC6, Geosci. Model Dev., 12(7), 2727–2765, doi:10.5194/gmd-12-2727-2019, 2019.

Thomason, L., Vernier, J.-P., Bourassa, A., Arfeuille, F., Bingen, C., Peter, T. and Luo, B.: Stratospheric Aerosol Data Set (SADS Version 2) Prospectus, to be Submitt. to Geosci. Model Dev. Discuss., n.d.

Thompson, G., Field, P. R., Rasmussen, R. M. and Hall, W. D.: Explicit Forecasts of Winter Precipitation Using an

25   Improved Bulk Microphysics Scheme. Part II: Implementation of a New Snow Parameterization, Mon. Weather Rev., 136(12), 5095–5115, doi:10.1175/2008MWR2387.1, 2008.

Tomita, H.: New microphysical schemes with five and six categories by diagnostic generation of cloud ice, J. Meteorol. Soc. Japan, 86A, 121–142, doi:10.2151/jmsj.86A.121, 2008.

Tomita, H. and Satoh, M.: A new dynamical framework of nonhydrostatic global model using the icosahedral grid, Fluid

30   Dyn. Res., 34(6), 357–400, doi:10.1016/j.fluiddyn.2004.03.003, 2004.

Tomita, H., Tsugawa, M., Satoh, M. and Goto, K.: Shallow Water Model on a Modified Icosahedral Geodesic Grid by Using Spring Dynamics, J. Comput. Phys., 174(2), 579–613, doi:10.1006/jcph.2001.6897, 2001.

Waliser, D. E., Li, J.-L. F., L'Ecuyer, T. S. and Chen, W.-T.: The impact of precipitating ice and snow on the radiation balance in global climate models, Geophys. Res. Lett., 38(6), n/a-n/a, doi:10.1029/2010GL046478, 2011.

Watanabe, S., Sato, K., Kawatani, Y. and Takahashi, M.: Vertical resolution dependence of gravity wave momentum flux simulated by an atmospheric general circulation model, Geosci. Model Dev., 8(6), 1637–1644, doi:10.5194/gmd-8-1637-2015, 2015.

Yamada, Y., Satoh, M., Sugi, M., Kodama, C., Noda, A. T., Nakano, M. and Nasuno, T.: Response of tropical cyclone
5 activity and structure to global warming in a high-resolution global nonhydrostatic model, J. Clim., 30(23), 9703–9724, doi:10.1175/JCLI-D-17-0068.1, 2017.

Yamada, Y., Kodama, C., Satoh, M., Nakano, M., Nasuno, T. and Sugi, M.: High-Resolution Ensemble Simulations of Intense Tropical Cyclones and Their Internal Variability During the El Niños of 1997 and 2015, Geophys. Res. Lett., 2019GL082086, doi:10.1029/2019GL082086, 2019.

10 Yamazaki, T., Taguchi, B. and Kondo, J.: Estimation of the heat balance in a small snow-covered forested catchment basin, Tenki (in Japanese), 41(2), 71–77, 1994.

Yang, W., Tan, B., Huang, D., Rautiainen, M., Shabanov, N. V., Wang, Y., Privette, J. L., Huemmrich, K. F., Fensholt, R., Sandholt, I., Weiss, M., Ahl, D. E., Gower, S. T., Nemani, R. R., Knyazikhin, Y. and Myneni, R. B.: MODIS leaf area index products: from validation to algorithm improvement, IEEE Trans. Geosci. Remote Sens., 44(7), 1885–1898,
15 doi:10.1109/TGRS.2006.871215, 2006.

Yashiro, H., Terai, M., Yoshida, R., Iga, S., Minami, K. and Tomita, H.: Performance Analysis and Optimization of Nonhydrostatic ICosahedral Atmospheric Model (NICAM) on the K Computer and TSUBAME2.5, in Proceedings of the Platform for Advanced Scientific Computing Conference on ZZZ - PASC '16, pp. 1–8, ACM Press, New York, New York, USA., 2016.

Tables

Table 1: List of HighResMIP simulations

Run name	Tier	Source ID	Horizontal mesh size	Initial atmospheric condition	Initial land condition	Integration period
g07f_1950	1 & 3	NICAM16-7S	56 km	ERA-20C (Poli et al., 2016)	NICAM climatology	1950–2050 (101-yr)
g08f_1950	1 & 3	NICAM16-8S	28 km	ERA-20C	NICAM climatology	1950–2050 (101-yr)
g09f_1950	1	NICAM16-9S	14 km	ERA-20C	NICAM climatology	1950–1960 (11-yr)
g09f_2000	1	NICAM16-9S	14 km	ERA-20C	NICAM climatology	2000–2010 (11-yr)
g09f_2040	3	NICAM16-9S	14 km	g08f_1950	g08f_1950 run, 1st January 2040	2040–2050 (11-yr)

Table 2: List of sensitivity experiments.

Experimental ID	Descriptions
g	Same as NICAM16-S.
g3	Same as g but for using the previous cloud microphysics scheme used in NICAM.12 (Table 7; Section 3.1).
g6	Same as g but for prescribing zero natural and anthropogenic aerosol mass concentration for the radiation scheme and constant CCN of 50 cm^{-3} for the cloud microphysics scheme (Section 3.3).
g4	Same as g but for omitting the effects of wetland and accumulation of water on land ice (Section 3.4).
g8	Same as g but for switching off the subgrid-scale orographic gravity wave drag scheme (Section 3.7).
g9	Same as g but for considering only the spherical particle in the radiation table (Section 3.2).
g9a	Same as g9 but for removing the interaction between radiation and cloud microphysics (Section 3.2).
f1d	Same as g but for a previous configuration of aerosol effective radii[#].
f1	Same as f1d but for using the previous SICCRT value of 300 kg m^{-2} (Section 3.6).
f	Same ad f1 but for using the previous surface albedo values (Table 8; Section 3.5).

In the f1d run, the aerosol effective radii of soil dust and seasalt are set to 4 μm and 2 μm, respectively, following the older MstrnX (Nakajima et al., 2000). In the g (=NICAM16-S) runs, those of soil dust and seasalt are set to 1.6 μm (Mahowald et al., 2014; Omar, 2005) and a function of relative humidity (considering hygroscopity).

Table 3: Physics schemes in NICAM16-S and NICAM.12

Model	NICAM16-S (NICAM.16 for CMIP6)	NICAM.12
Cloud microphysics	NICAM Single-moment Water 6 (NSW6) (Tomita, 2008; Roh and Satoh, 2014; Roh et al., 2017)	NSW6 (Tomita, 2008; Kodama et al., 2012)
Cumulus convection and laege-scale condensation	Not used	Not used
Radiation	MstrnX (Sekiguchi and Nakajima, 2008), updated radiation table (Seiki et al., 2014), and coupling with cloud microphysics	MstrnX (Sekiguchi and Nakajima, 2008)
Turbulence	Mellor-Yamada Nakanishi-Niino (MYNN2) (Nakanishi and Niino, 2006; Noda et al., 2010)	Same
Gravity wave	Orographic gravity wave drag (McFarlane, 1987)	Not used
Land surface	Minimal Advanced Treatments of Surface Interaction and RunOff (MATSIRO) (Takata et al., 2003) with wetland scheme (Nitta et al., 2017) and albedo modification	MATSIRO (Takata et al., 2003)
Ocean surface flux	Bulk surface scheme (Louis, 1979); surface roughness is evaluated following Fairall et al. (2003) and Moon et al. (2007)	Same
Ocean model	Fixed to observation (or single layer slab ocean with a nudging toward observation)	Single layer slab ocean with a nudging toward observation

Table 4: List of observational datasets

Short name	Full name	Resolution	Reference
CERES	Clouds and Earth's Radiant Energy System (CERES) Energy Balanced and Filled (EBAF) TOA/SFC Edition 4.0 (Ed4.0)	1.0°×1.0°, monthly-mean	Kato et al. (2018), Loeb et al. (2018)
CloudSat	CloudSat level 2B radar-only cloud water content (2B-CWC-RO)	0.25°×0.25°	Austin et al. (2009), Austin and Stephens (2001)
GPCP	Global Precipitation Climatology Project (version 2.2)	2.5°×2.5°, monthly-mean	Adler et al. (2003)
GridSat	Gridded Satellite Data – B1	0.07°×0.07°, three-hourly	Knapp et al. (2011)
ISCCP	International Satellite Cloud Climatology Project	2.5° × 2.5°, monthly-mean	Rossow and Schiffer (1999)
JRA-55	Japanese 55-year reanalysis	1.25° × 1.25°, monthly-mean	Kobayashi et al. (2015)

Table 5: Global mean impacts of the model updates. They are averaged over June 2004 – May 2005.

	a. Modification of cloud microphysics (3.1)		b. Introduction of aerosol (3.3)		c. Modification of surface albedo (3.5)	d. Modification of SICCRT (3.6)	e. Impact of slab ocean (3.6)			f. Introduction of orographic gravity wave drag (3.7)
Experimental ID (Table 2)	g-g3		g-g6		f1-f	f1d-f1	g	g	g	g-g8
Horizontal mesh size	14 km*	56 km	14 km*	56 km	56 km	56 km	56 km	28 km	14 km	56 km
Surface air temperature, ℃	-0.30	-0.10	-0.04	-0.06	+0.08	-0.21	+0.10	+0.15	+0.15	-0.16
Precipitation, mm day^{-1}	+0.08	+0.08	-0.02	-0.02	+0.04	-0.01	+0.02	+0.03	+0.02	-0.01
TOA OLR, W m^{-2}	+4.47	+4.03	+0.01	-0.02	-0.52	-0.47	+0.30	+0.27	+0.34	-0.24
TOA OSR, W m^{-2}	-2.52	-1.83	-2.17	+0.24	-2.03	+0.05	+0.07	+0.38	+0.60	-0.01
IWP, g m^{-2}	+46.03	+51.24	-0.74	-0.67	+0.26	-0.04	-0.19	-0.51	-0.75	-0.23
LWP, g m^{-2}	+0.50	+0.09	-4.14	-2.58	+1.07	-0.33	+0.31	+1.13	+1.19	-0.28
ISCCP high visible cloud amount, %	-6.25	-5.35	+0.09	-0.12	-0.28	+0.07	+0.17	+0.19	+0.16	-0.09
ISCCP middle visible cloud amount, %	+0.28	+1.03	+0.09	-0.04	+0.18	+0.06	+0.10	+0.20	+0.34	-0.06
ISCCP low visible cloud amount, %	+1.81	+1.89	-0.85	-0.35	+0.59	-0.03	-0.47	-0.33	-0.20	+0.18
SFC net LW, downward pos., W m^{-2}	+0.40	+1.03	+0.61	+0.67	+2.00	+0.26	+0.37	+0.69	+0.73	+0.07
SFC net SW, downward pos., W m^{-2}	+1.23	+0.44	-0.25	-2.68	+2.12	-0.00	-0.32	-0.79	-1.07	+0.07
SFC latent heat flux, upward pos., W m^{-2}	+2.19	+2.35	-0.61	-0.66	+1.16	-0.33	+0.70	+1.04	+0.75	-0.38
SFC sensible heat flux, upward pos., W m^{-2}	+1.03	+1.07	-1.24	-1.20	+0.25	+0.17	-0.11	-0.15	-0.15	+0.37

*slab ocean model with nudging toward the SST boundary condition is used instead of fixed SST condition.

Table 6: Global mean comparison between NICAM.16-S simulations and observations. Average over June 2004 – May 2005.

	NICAM16-S			Observations
CMIP6 formal model label (if any)	NICAM16-7S	NICAM16-8S	NICAM16-9S	
Horizontal mesh size	56 km	28 km	14 km	
Surface air temperature, ℃	14.32	14.20	13.78	14.59a
Precipitation, mm day^{-1}	2.96	2.88	2.85	2.71b
TOA OLR, W m^{-2}	238.12	237.66	235.52	240.20c
TOA OSR, W m^{-2}	83.48	82.20	91.33	99.11c
IWP, g m^{-2}	88.44	87.86	81.55	
LWP, g m^{-2}	43.02	39.37	46.35	
ISCCP high visible cloud amount, %	21.54	23.23	22.73	22.58d
ISCCP middle visible cloud amount, %	11.67	11.16	13.32	20.04d
ISCCP low visible cloud amount, %	10.73	10.18	16.95	23.17d
SFC net LW, downward pos., W m^{-2}	-59.12	-60.23	-56.61	-52.91c
SFC net SW, downward pos., W m^{-2}	184.32	186.06	176.48	163.87c
SFC latent heat flux, upward pos., W m^{-2}	85.82	83.44	82.67	
SFC sensible heat flux, upward pos., W m^{-2}	17.58	18.80	20.63	

a: JRA55. b: GPCP. c: CERES. d: ISCCP.

Table 7: Summary of the key changes in the NSW6 scheme by Roh and Satoh (2014) and Roh et al. (2017)[#].

		NSW6 in NICAM.16-S (Roh and Satoh, 2014; Roh et al., 2017)	NSW6 in NICAM.12 (Tomita, 2008; Kodama et al., 2012)
a.	Production of cloud ice	Ice nucleation and vapor deposition are calculated explicitly following Hong et al. (2004).	Cloud water and cloud ice are produced or reduced by saturation adjustment (Tomita, 2008).
b.	Terminal velocity of cloud ice (no change between the two)	0	0
c.	Size distribution of snow	A bi-modal shape of the rescaled particle size distribution of snow is assumed following Thompson et al., (2008), who used aircraft observations by Field et al. (2005).	Marshall Palmer distributions are assumed for rain, snow, and graupel with global constants of N_0 following Lin et al. (1983) and Rutledge and Hobbs (1984), as follow: $N_j(D_j) = N_{0,j}\exp(-\lambda_j D_j), (j = r,s,g)$.
d.	Mass and diameter (M-D) relationship of snow	The mass (m) and maximum dimension (D) relationship of snow assumes two-dimensional fractal shapes ($m_s = 0.069\,D_s^2$) with variable snow density following Thompson et al., (2008).	Ice hydrometeors are assumed as the spherical shape with fixed bulk densities following Rutledge and Hobbs (1984).
e.	Intercept parameter in the M-D relationship of graupel	The intercept parameter of graupel $N_{0g} = 4 \times 10^8$ [m^{-4}] is used (Gilmore et al., 2004; Knight et al., 1982)	The intercept parameter of graupel $N_{0g} = 4 \times 10^6$ [m^{-4}] is used following Rutledge and Hobbs (1984), assuming midlatitude cyclones.
f.	Accretion of snow and cloud ice by graupel	Accretion of snow and cloud ice by graupel is ignored following Lang et al. (2007).	Accretion of snow and cloud ice by graupel occurs.
g.	Efficiency of accretion of cloud ice by snow	0.25.	1.0.

The particle size distribution of rain was also revised in the original paper, but the revision is not used in the latest version
because of computational efficiency against its small impact on improvements. In addition, the assumption that cloud ice
5 does not precipitate is inconsistent with some ice cloud microphysics but is used to reproduce observed high cloud signals
over the tropics ad hoc.

Table 8: Surface albedo in NICAM16-S and NICAM.12.

	NICAM16-S	NICAM.12
Sea ice, VIS and NIR	0.5 and 0.5 (Hashino et al., 2016)	0.8 and 0.6
Snow over sea ice, IR	0.02 (Armstrong and and Brun, 2008; Niwano et al., 2014)	0
Fresh snow over land, VIS	0.90 (e.g. Aoki et al. 2011; Yamazaki et al. 1994)	0.98
Open ocean, IR	0.05	0.005

VIS, NIR, and IR stand for visible, near-infrared, and infrared bands, respectively.

Table 9: Technical aspects of the simulations on the Earth Simulator 3. They are sampled from 6-month simulations (1 July 2004–31 December 2004).

Source ID	NICAM16-7S	NICAM16-8S	NICAM16-9S
Number of nodes	10	40 / 160	160
Number of MPI processes	40	160 / 640	640
File staging	No	Yes / Yes	Yes
Simulation year per wall-clock day (SYPD)	0.42	0.37 / 0.63	0.22
Output size in latitude-longitude grid per year, TB	0.64	2.4	9.5

Figures
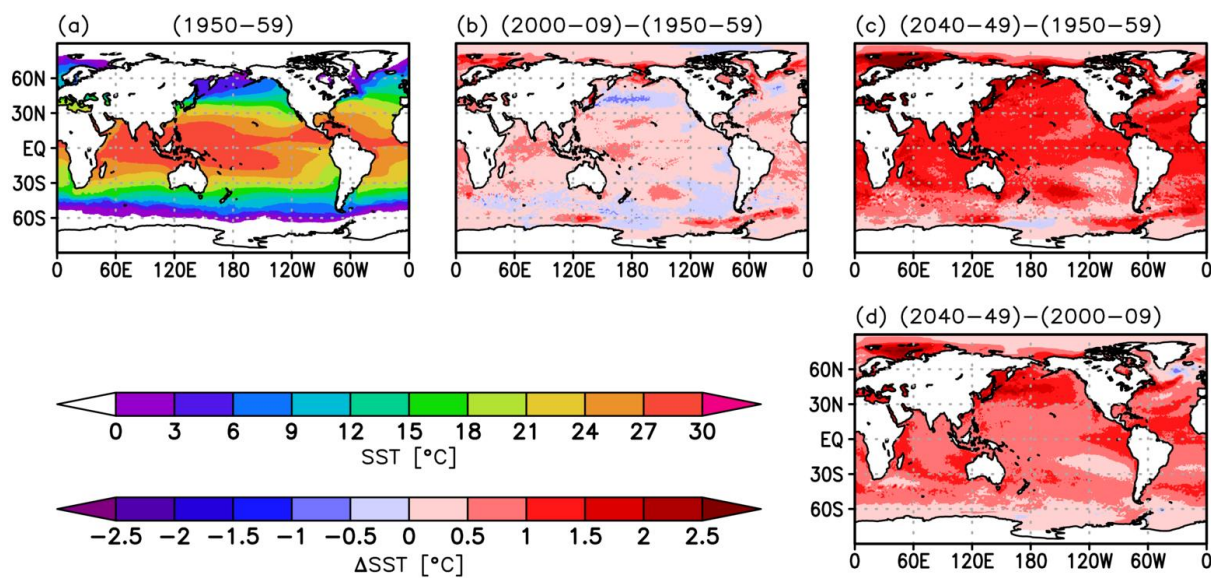
Figure 1: Decadal mean horizontal distribution of sea surface temperature (SST) prescribed for the model averaged in the 1950s (a). Differences between the 2000s and the 1950s (b), the 2040s and the 1950s (c), and the 2040s and the 2000s (d) are also shown.
5 **Their unit is in degrees Celsius.**
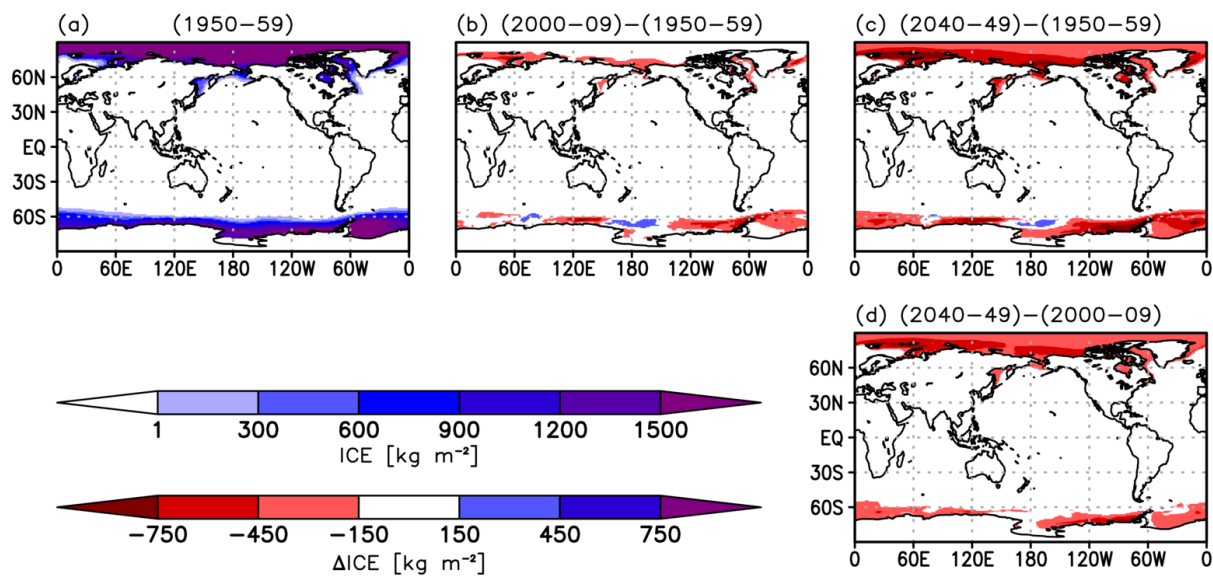
Figure 2: The same as Figure 1 but for sea ice mass (ICE) in kg m⁻².
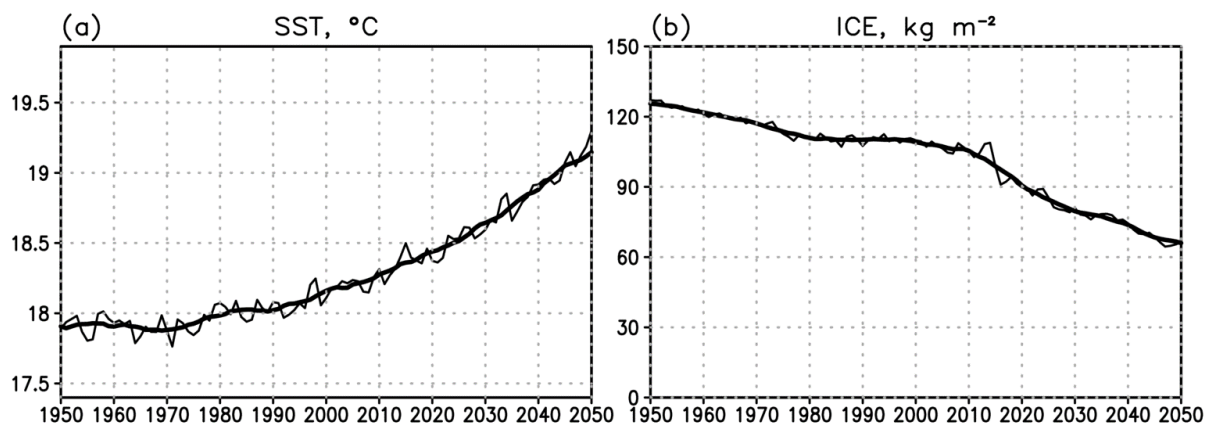
Figure 3: Global mean SST (a; in °C) and ICE (b; in kg m⁻²) prescribed for the model. Annual (thin line) and decadal (thick line) means are shown.
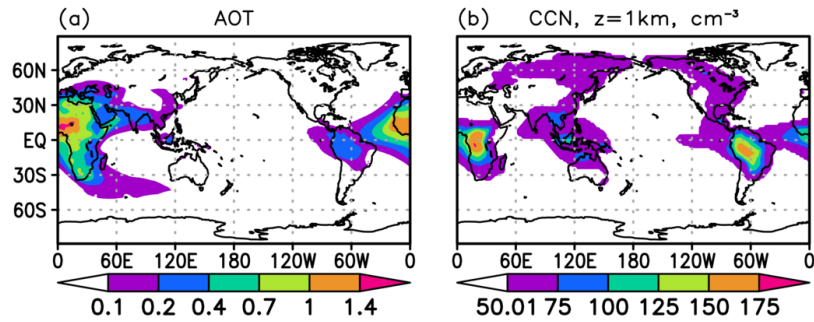
Figure 4: (a) Annual mean natural aerosol optical thickness simulated by NICAM16-7. The simulation, starting from 1 June 2004, was conducted for one year without anthropogenic aerosol. (b) The annual mean number concentration of cloud condensation nuclei (CCN) from the natural origin at 1 km above sea level prescribed for the model. The unit is cm^{-3}, The lower bound of CCN is 50 cm^{-3}.
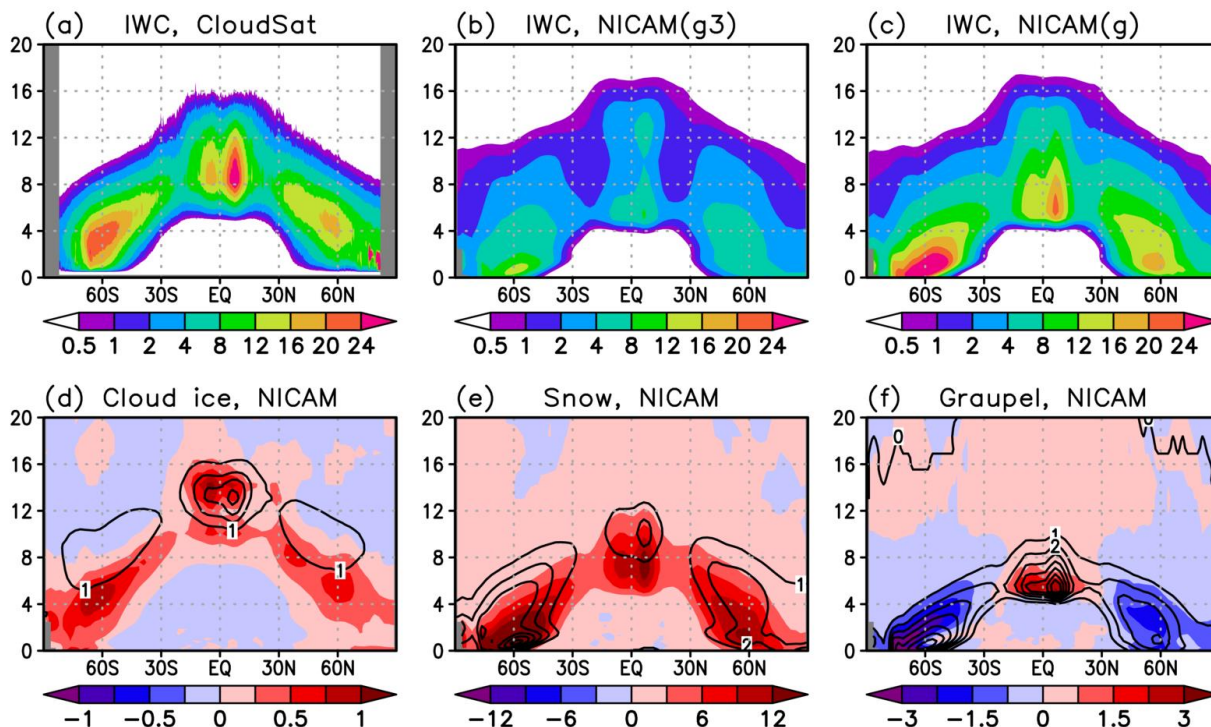
Figure 5: Annual mean of the zonal mean ice water content (IWC; unit in 10^{-6} kg m^{-3}) in CloudSat observation (a), and 14 km mesh NICAM simulations using the cloud microphysics scheme of NICAM.12 (b) and that of NICAM16-9S (c) (Table 7; g3 and g runs in Table 2). Breakdown of the simulated IWC into cloud ice (d), snow (e), and graupel (f) is shown on the bottom panels. The contour shows the simulation using the cloud microphysics schemes before the update and shading shows the difference between the simulations using the cloud microphysics schemes before and after the update. The analysis data are 0.25° (a) and 2.5° (b–f) gridded data, and the vertical axis is the altitude above sea level.
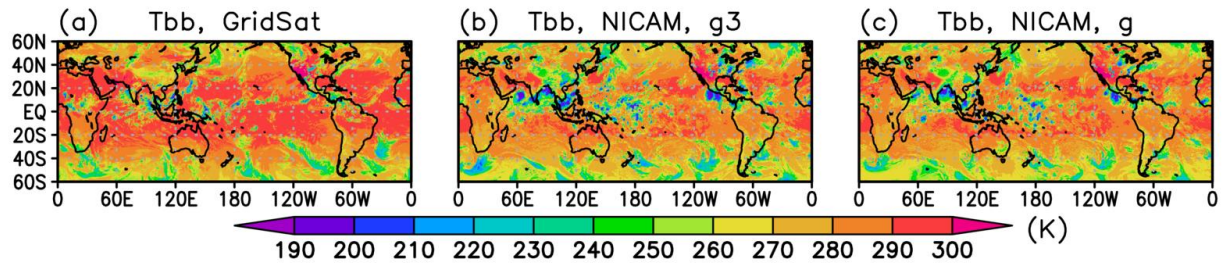
Figure 6: Top-of-the-atmosphere (TOA) brightness temperature near 11 μm at 00:00 UTC June 6, 2004, from GridSat product (a) and NICAM using the cloud microphysics scheme of NICAM.12 (b; g3 run in Table 2) and that of NICAM16-9S (c; g run in Table 2). The display style follows Figure 1 of Roh et al. (2017). Grid interval of the NICAM data is 0.14°.
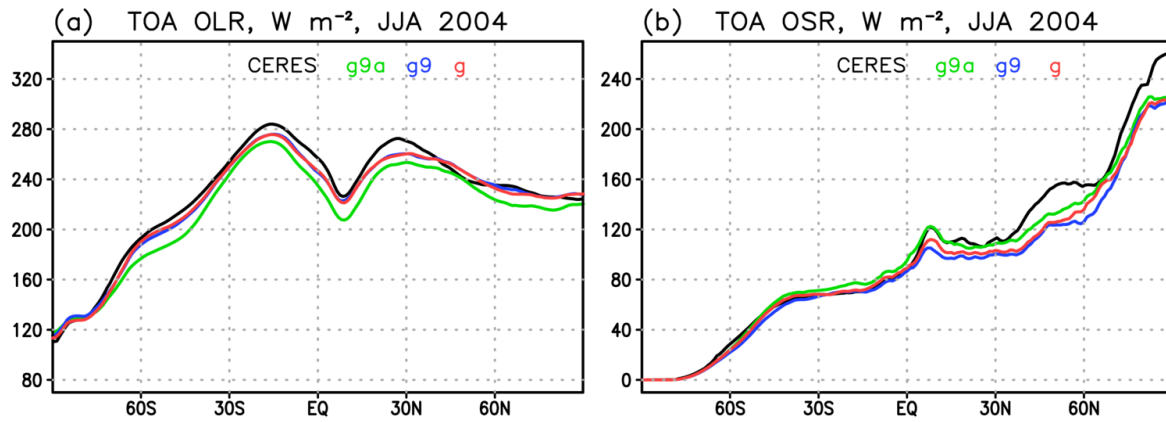
Figure 7: TOA outgoing longwave radiation (OLR) (a) and outgoing shortwave radiation (OSR) (b), in W m⁻², averaged over June-July-August in 2004 for CERES product (black) and 14 km mesh NICAM simulations. Green, blue, and red lines show g9a, g9, and g runs in Table 2.
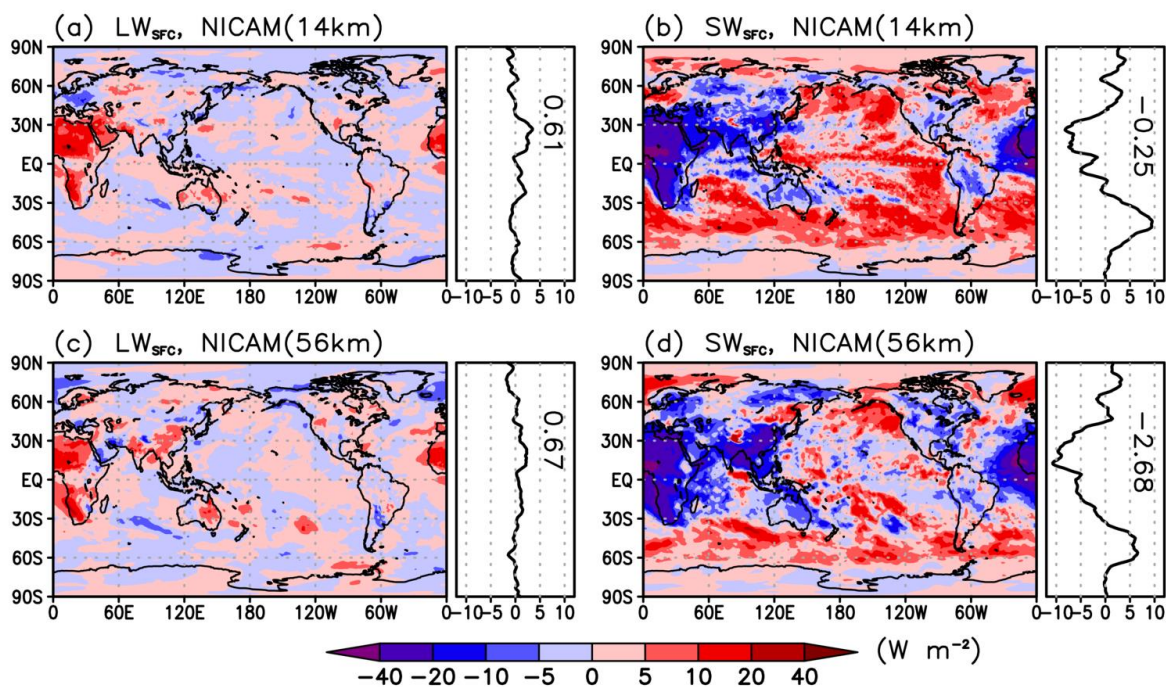
Figure 8: Impact of the update of the aerosol treatment described in Section 3.3 (g–g6 in Table 2). 2-D distribution, zonal, and global means of the net longwave (left) and shortwave (right) radiation at the surface are shown for the 56 km (top) and 14 km mesh simulations (bottom). The sign of the radiation is downward positive.
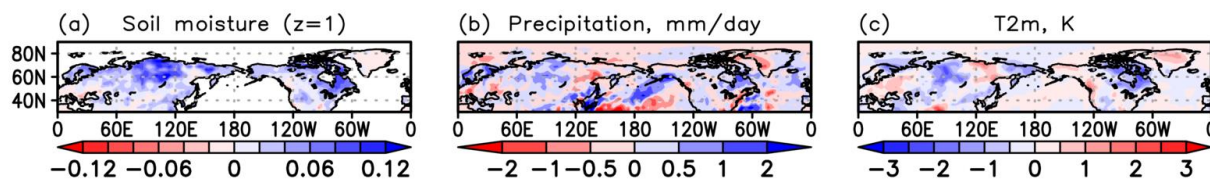
Figure 9: Impact of the update of the land model described in Section 3.4 and Table 2 (g4–g) on the simulated soil moisture at the uppermost model level (a), precipitation (b), and surface air temperature (c). Simulations using 56 km NICAM were performed for four years, and last three June-July-August data are averaged.
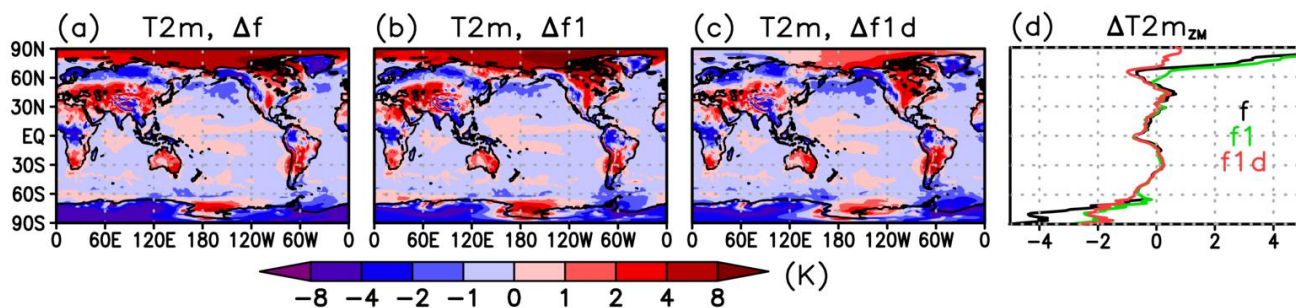
Figure 10: Bias in the simulated surface air temperature (K) against JRA-55 reanalysis averaged for June 2004 – May 2005. (a) Old albedo configuration and SICCRT = 300 (the f run in Table 2). (b) New albedo configuration and SICCRT = 300 (the f1 run in Table 2). (c) New albedo configuration and SICCRT = 1600 (the f1d run in Table 2). (d) The zonal mean bias of the surface air temperature.
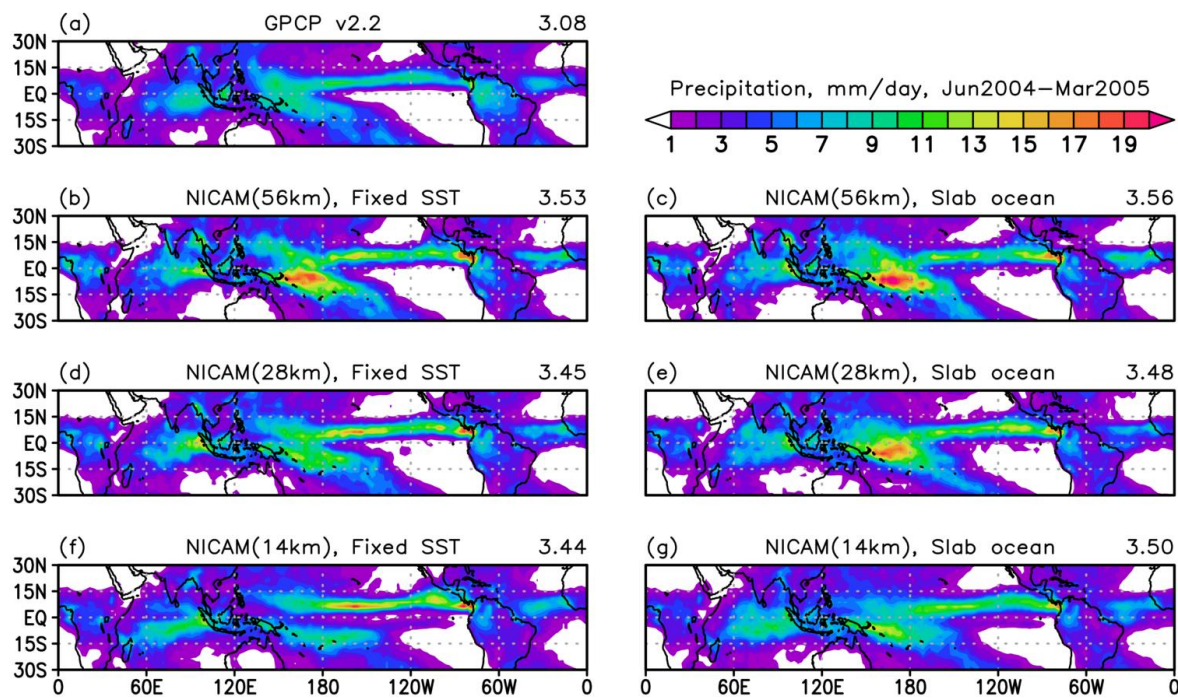
Figure 11: Annual mean precipitation during June 2004 – May 2005 for GPCP (a), NICAM with the SST boundary condition fixed to the prescribed SST (c, e, g), and NICAM with the slab ocean model nudged toward the prescribed SST (d, f, h). Results from NICAM16-7S (c, d), NICAM16-8S (e, f), and NICAM16-9S (g, h) are shown, and tropical mean precipitation are noted at the top-right of each panel.
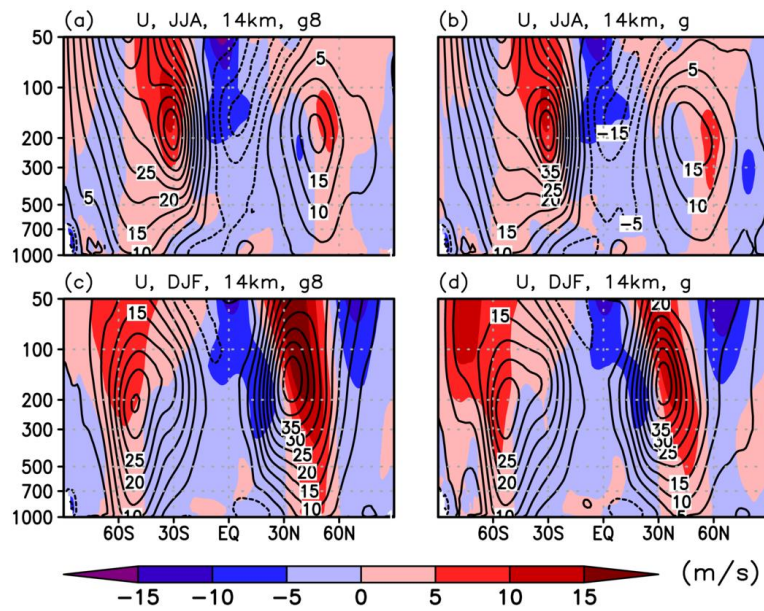
Figure 12: Zonal mean zonal wind (contour) and its bias from JRA-55 reanalysis (shaded) for June – August 2004 (a, b) and December 2004 – February 2005 simulated by 14 km mesh model without (a, c) and with the gravity wave drag scheme (b, d).
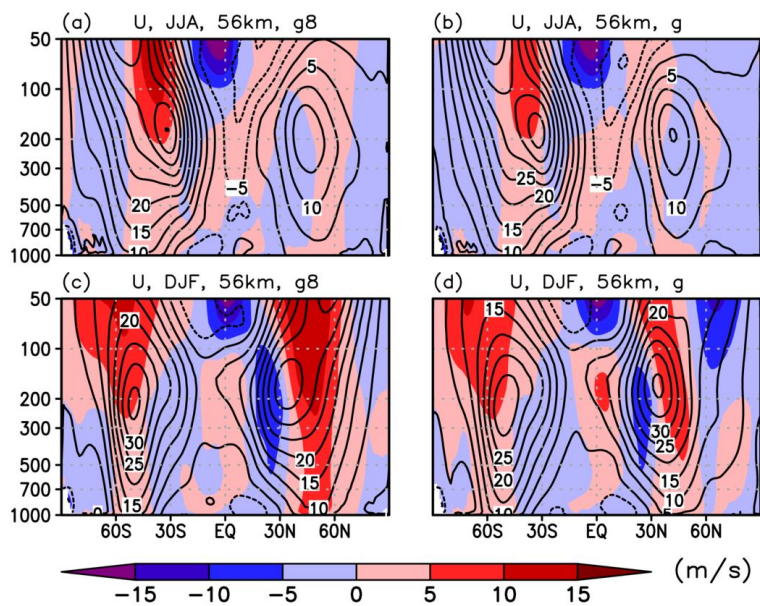
Figure 13: Same as Figure 12 but for the simulation by 56 km mesh model.
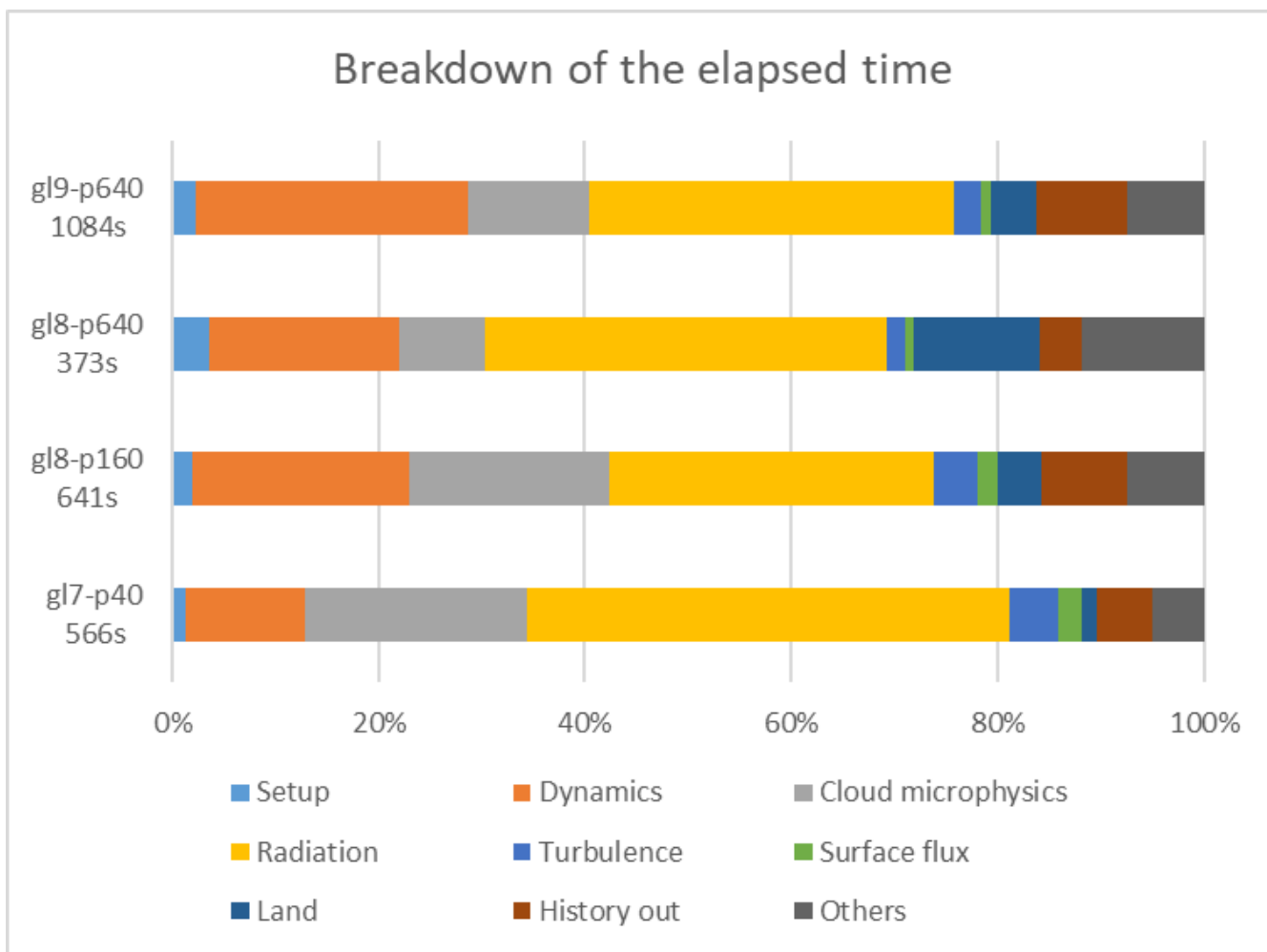
Figure 14: Percentage of the elapsed time for each component on the Earth Simulator 3. They are sampled from 6 month simulations (1 July 2004–31 December 2004). The computational time per 1 day integration is shown on the left.